MULTILEVEL COMPOSITION: AN INNOVATIVE RGB-BASED TECHNIQUE FOR ELUCIDATING SUBTLE CONNECTIONS BETWEEN INTRICATE GEOLOGICAL FEATURES ON THREE-DIMENSIONAL SEISMIC REFLECTION DATA

Muhedeen Lawal[1], Ingo Pecher[2,3], Or. M. Bialik[1,4], Nicolas D. Waldmann[1], Joerg Bialas[5], Zvi Koren[6], Yizhaq Makovsky[1,7*]

1. Dr. Moses Strauss Department of Marine Geosciences, Charney School of Marine Sciences (CSMS), University of Haifa, Haifa 3498838, Israel.
2. Department of Physical and Environmental Sciences, Texas A&M University – Corpus Christi, TX 78412, USA.
3. School of Environment, University of Auckland, Auckland 1142, New Zealand.
4. Department of Geosciences, University of Malta, Msida MSD 2080, Malta.
5. Marine Geodynamics, GEOMAR Helmholtz Centre for Ocean Research Kiel, 24148 Kiel, Germany.
6. Emerson, Gav-Yam, 46120, Herzeliya, Israel.
7. Hatter Department of Marine Technologies, CSMS, University of Haifa, Haifa 3498838, Israel.

*Corresponding Author

Muhedeen Lawal: muhedeenlawal@gmail.com

Ingo Pecher: ingo.pecher@tamucc.edu

Or. M. Bialik: obialik@campus.haifa.ac.il

Nicolas D. Waldmann: nwaldmann@univ.haifa.ac.il

Joerg Bialas: jbialas@geomar.de

Zvi Koren: Zvi.Koren@emerson.com

Yizhaq Makovsky: yizhaq@univ.haifa.ac.il

Abstract

Advanced seismic data and multi-attribute visualization techniques such as the red-green-blue (RGB) have considerably augmented the capability of interpreters to characterize geological features on three-dimensional (3D) seismic reflection datasets. However, high resolution investigation of complex features remains challenging, requiring additional approaches to improve all round interpreters' performance. Intervals of interest are commonly associated with intricate geological features, including channel systems and fluid migration pathways, which may be concealed in the dataset as multilevel high-amplitude seismic reflectivity bands. Delineating such features onto a single, intuitive map is often an arduous task. This may prove even more demanding where such features are spatially connected and occur near discontinuous and difficult-to-interpret horizons. To aid this task, we have developed an innovative technique involving RGB-blending and composition of multilevel amplitude maps, multilevel composition. Multilevel composition involves identification of high-amplitude features of geological interest within the dataset and defining their window of occurrence. This is followed by the interpretation of at least one reflecting horizon within/around the target window and the division of the window into three sub-windows based on the spatiotemporal distribution of the geological features. Amplitude-accentuating seismic attributes are computed for the sub-windows, the resulting maps are assigned to red (shallowest level), green (intermediate level) and blue (deepest level) colors and are co-rendered in the RGB color space. This results in a single map in which inter-window/layer depth information is coded in colors for reliable representation of the actual geology. We demonstrate the efficacy of this technique by applying it to characterize classic deep-water depositional elements in the eastern Nile fan, eastern Mediterranean, and to investigate seafloor seeps and underlying fluid plumbing systems beneath the Omakere Ridge, offshore New Zealand, using high-resolution 3D seismic

data. The new technique is simple and easy to execute and enhances existing seismic interpretation workflows.

Keywords: Multilevel composition, RGB blending, multi-attribute visualization, 3D seismic data, Seismic interpretation, subsurface characterization, seafloor habitats, Nile fan, Omakere Ridge.

1. Advances in seismic interpretation techniques

Unravelling the huge amount of information contained in seismic reflection images for obtaining an in-depth understanding of the subsurface geology and to build detailed of structural/stratigraphic models, is the main goal of seismic interpretation (e.g., Henderson et al., 2008; Bacon et al., 2010). In recent years, the petroleum industry has witnessed improved seismic interpretation capabilities. Most of these improvements are driven by significant advancement in workstation capabilities, development of innovative imaging algorithms and methodologies, improved artificial intelligence and machine learning capabilities, and advanced visualization techniques (e.g., Cartwright and Huuse, 2005; Zeng, 2010; Cao et al., 2016; Di et al., 2019; Zheng et al., 2019; Kumar and Sain, 2020). Many of these improvements have become possible owing to the development of a wide range of volumetric seismic attributes that generally form a key part of integrated seismic interpretation workflows. Different types of seismic attributes have been designed to enhance specific geological characteristics within the seismic images (e.g., Chopra and Marfurt, 2007; Henderson et al., 2008). Such useful geological information can be visualized through two-dimensional (2D)/map-based attribute displays, preferably through high fidelity 3D multi-attribute display techniques such as the RGB color model (Henderson et al., 2008), volume rendering (Alves et al., 2015; Chaves et al., 2011) and geobody extraction (Chaves et al., 2011).

The RGB color model makes it possible to create multi-attribute displays with greater clarity and detail than simple monochromatic attribute displays.

Volumetric co-rendering of multiple attributes using the RGB color model is widely used to visualize subsurface geological features (Henderson et al., 2008; Stark, 2006), with its most common use being in the co-rendering of frequency volumes derived from spectral decomposition (Partyka et al., 1999). The use of the RGB color model for geological visualization has been conventionally limited to volume-based attribute displays. When interpreters are faced with the task of characterizing multilevel geological features from seismic datasets, a volume-based approach may not always be sufficient to image the full extent of the geological features and to establish any connection between them. This could be even more challenging if (1) There are no continuous and easy-to-interpret horizons around the features, as an interpretable horizon is a prerequisite for horizon-based attribute computation, or (2) When seismic attributes, resulting from multiple intervals, are to be presented in a single, intuitive map. This limitation is also inherent in the output display of the spectral decomposition technique in that only features from a single interval or a slice can be displayed at a given time on a given resulting map. To resolve this difficulty, we propose a technique that incorporates geological features from multiple subsurface depth intervals into a single map, demonstrating its advantages in enriching the visualization of fine structural and stratigraphic geological features that were hidden to the interpreters when using conventional methods.

The seismic amplitude is the primary attribute of all seismic reflection images (Brown, 2001; Chopra and Marfurt, 2007) and when anomalous features are found, a workflow that incorporates amplitude-accentuating attributes can be designed to efficiently map them. This paper describes a technique to enhance the visualization of high amplitude multi-depth/-level geological features using their composed amplitude characteristics. This technique, which we name "multilevel composition" provides co-rendered versions of multilevel attribute maps and it has been proven to be an effective visualization and characterization approach in the seismic interpretation workflow. This paper starts with a detailed methodology section, illustrating the multilevel composition technique, followed by two case studies. We visualize (a) Deep-water depositional elements such as channels in 3D seismic images, generated for hydrocarbon exploration in the Levant Basin, eastern Mediterranean, and (b) Seafloor cold seeps and associated deeper gas-bearing intervals using high-resolution 3D seismic images based on a P-Cable survey from the Omakere Ridge, offshore New Zealand.

2. Datasets and methods

The first application, presented here, of the multilevel composition technique is based on the western half of the Sara-Myra 3D seismic data, acquired over parts of the eastern deep-sea fan of the Nile in water depths of ~1100 m to ~1500 m in the Levant Basin (Figure 1a). Technical details of the dataset are available in Table 1. Processing procedures applied to the data include band pass filtering, diffraction-multiples removal, normal move-out correction, fold normalization, spatial anti alias filtering, amplitude preservation techniques, and 3D Kirchhoff prestack depth migration. Such a processing sequence is an industry-standard for amplitude preserving imaging, though not rigorously "true amplitude". The second case study describes the application of the proposed multilevel composition over a 3D seismic image obtained from a high-resolution P-cable 3D seismic dataset, acquired over an area of 2 km x 7 km on the Omakere Ridge (Figure 1b). The dataset was acquired perpendicular to the axis of the ridge using sixteen streamers attached at 10 m spacing and a 4.2 L GI-gun deployed at 2 m water depth. Technical details of the recorded seismic dataset are available in Table 1. The processing procedures applied to the data include CMP binning, band pass filtering, deconvolution to attenuate seafloor ghosts, tide and residual static corrections, amplitude preservation and 3D Kirchhoff time migration. Although the processing procedures applied to the two datasets are not exhaustively discussed in this study, they nonetheless enhanced their signal to noise ratio and reduced the amplitude distortions, thus preconditioned them for attribute computation and for the proposed multilevel composition. All the analyses performed on the datasets were carried out in the depth (meters) domain for the Sara-Myra dataset and in vertical time (milliseconds) for the Omakere dataset. Emmerson's Paradigm software was used to analyze and interpret the seismic datasets. Particularly, the RGB composition capabilities embedded in this software package were exploited to execute the multilevel composition technique, as they permit advanced blending of multi-attribute 2D maps.

Table 1. Technical details of the datasets used in this study.

Survey name	Acquisition details	Type and unit	Technical details	Additional details
Sara-Myra	Acquired by CGG-Veritas Year: 2001	Industry standard Depth Migrated 3D Seismic reflection, Depth in meters	Bin size: 6.25 m x 25 m Sampling interval: 2 ms Inline and Crossline spacing: 25 m and 12.5 m Vertical and horizontal resolution: ~6 m	Zero phase Display: Society of Exploration Geophysicists (SEG) Normal Polarity convention.
Omakere	Acquired during SO-214 cruise Year: 2011	P-Cable Time Migrated 3D Seismic reflection, TWT seconds	Bin size: 6.25 m x 6.25 m Sampling interval: 0.25 ms Inline and Crossline spacing: 6.2 m and 6.2 m Vertical and lateral resolution: ~6.25 m and ~6.25 m	Zero phase Display: SEG Normal Polarity convention.

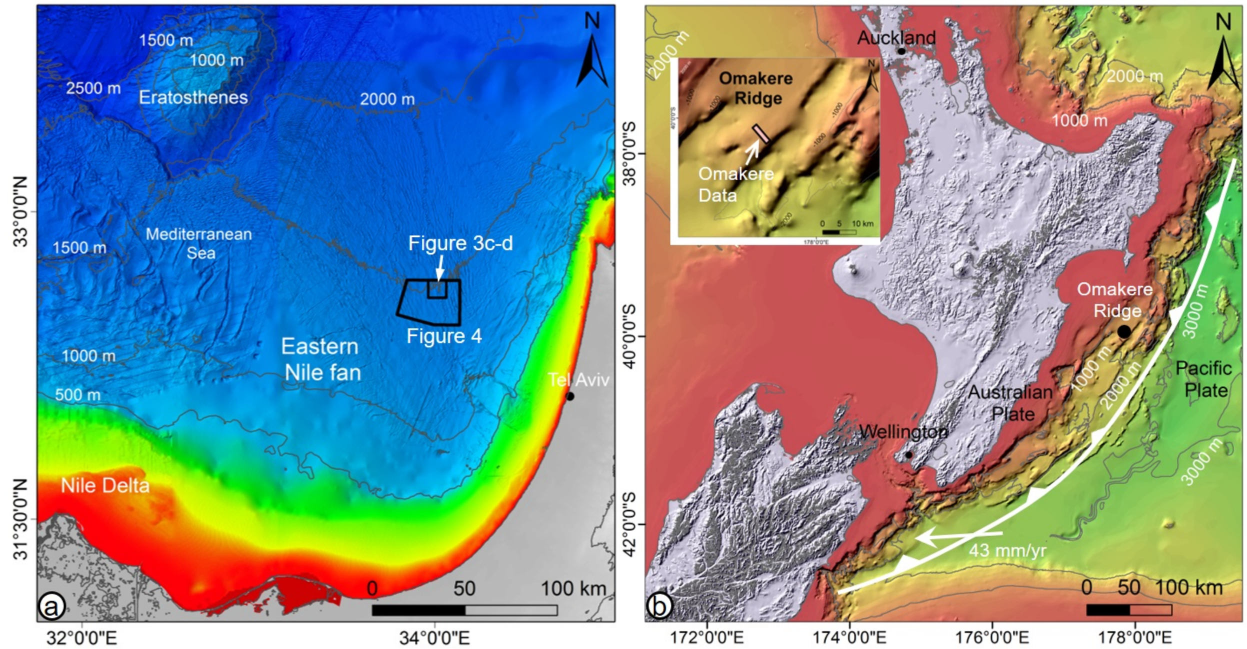

Figure 1. Color-coded and contoured bathymetry of the case study areas. (a) The eastern deep-sea fan of the Nile river in the eastern Mediterranean (from EMODNET and GEBCO websites), overlaid with the outline of the Sara-Myra 3D seismic data. (b) Omakere Ridge, offshore New Zealand (from NIWA website), overlaid with the outline of the Omakere 3D seismic data.

3. The Multilevel Composition technique

3.1 Attribute selection and expression

As mentioned, seismic attributes refer to quantitative measures of certain characteristics of a seismic dataset and are used to enhance geological or geophysical interpretation of the subsurface (Brown, 2001; Chopra and Marfurt, 2007). An interpreter's choice of the attributes to be selected generally depends on the principal geological features of interest and the interpreter's experience in the studied area. For instance, amplitude, envelope and instantaneous frequency/phase attributes are known as lithology and fluid indicators (Chopra and Marfurt, 2007). Geometric attributes, such as structural dips/azimuths and curvatures quantify the reflectors geometry (Chopra and Marfurt, 2006). Coherence measures are also important geometric attributes in revealing faults and discontinuities in 3D seismic images (Bahorich and Farmer, 1995). Since the objective of this paper is to delineate fine (hidden) geological features (e.g., channels, splays, and seeps), most of which are characterized by high amplitude anomalies, we first computed the amplitude-accentuating attributes such as signal envelope, root mean square (RMS) and maximum positive amplitude that clearly allow for delineating these features from the surrounding background. The signal envelope (E) or reflection strength attribute represents the instantaneous energy of the seismic signal (Chopra and Marfurt, 2005) and is mathematically derived from the complex trace (Taner et al., 1979) by:

$$E(t) = \sqrt{\{T^2(t) + H^2(t)\}} \qquad (1)$$

where T(t) is the original seismic trace and H(t) is its Hilbert's transform (e.g., Subrahmanyam and Rao, 2008). It reveals only positive amplitudes and is commonly used in revealing changes in deposition and lithology, tuning effects and sequence boundaries (Subrahmanyam and Rao, 2008). The envelop is used in this study to delineate buried depositional features such as channels and splays. The RMS amplitude is the square root of the sum of the weighted seismic amplitudes (x) squared, normalized by the number of samples, N, within the time window of interest (w and n) (Chopra and Marfurt, 2008; Koson et al., 2014). It is mathematically presented as:

$$x_{rms}\sqrt{\frac{1}{N}\left(\sum_{n-1}^{N} w_n x_n^2\right)} \qquad (2)$$

As the RMS amplitudes combine the effect of both positive and negative amplitudes, they are responsive to fluids or sandstone-bearing depositional systems (Brown, 1991). This attribute is used in this work to delineate subsurface features that could represent fluid/gas-bearing intervals. Furthermore, the maximum positive amplitude is the peak amplitude of the positive portion of the seismic trace. Hence, it is suitable for delineating features that are characterized by positive amplitudes (Chopra and Marfurt, 2007). Seafloor seepage-related features such as denser sediments, authigenic carbonates, shell debris and gas hydrates are normally associated with positive amplitudes (Judd and Hovland, 2007; Roberts et al., 2006). Consequently, the maximum positive amplitude attribute is used in this study to delineate seafloor and near seafloor indicators of gas seeps.

3.2 RGB color model

Color models like the RGB, hue-saturation-value (HSV) and cyan-magenta-yellow (CMY) are color spaces where the color is defined by a 3D coordinate system based on specific spectral windows along the visual spectrum. (Al-Shuhail et al., 2017; Cao et al., 2016; Marfurt, 2015). Amongst these models, the most widely used by the geoscientists is the RGB. This is mainly because most of the computer and television screens are equipped with the red, green, and blue color components (Al-Shuhail et al., 2017). The RGB is an additive color model that mixes the three primary colors: red, green and blue, in various ways to produce a variety of colors that are visible and appealing to the human eyes (Figure 2). The composing primary colors generally have varying intensities ranging from low (0) to high (255) and their intermixing produces secondary colors (Figure 2). The nature of the secondary colors depends on the intensity of each primary color component in the RGB color space (Cao et al., 2015). In 3D, the red, green, and blue colors are commonly mapped onto the x, y, and z-axes respectively, and when each color component is set to zero (0, 0, 0), their intermixing produces the darkest color which is black. Setting each component to the highest value (255, 255, 255) produces the brightest color which is white (Cao et al., 2015). Additive blending of red and green colors produces yellow (255, 255, 0), blending of red and blue colors produces magenta (255, 0, 255) and blending of green and blue colors produces cyan (0, 255, 255) (Figure 2). Each color component/channel in the RGB model can represent up to 8 bits of information, producing a blend with an overall color depth of 24 bits or $(2^8)^3$ or 16,777,216 colors. This provides the basis for the high level visualization, resulting from the RGB model (Al-Shuhail et al., 2017; Cao et al., 2015). Notwithstanding, reliable geological interpretations are determined by proper understanding of the complex color outputs of the RGB space and the ability to separate noise from useful information.

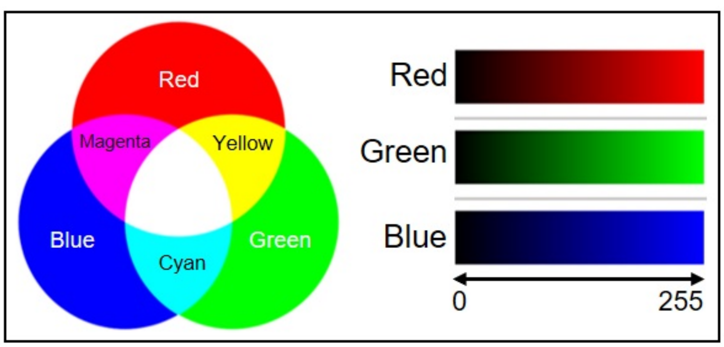

Figure 2. The RGB color model (left) and the RGB color space layers (right) used by us.

3.3 Multilevel composition via RGB blending

Proper visualization of seismic attributes involves the ability to identify and distinguish geological features and their characteristics on seismic attributes. This ability is essential for optimal characterization of the multilevel high amplitude geological features from 3D seismic images. To ensure proper visualization and characterization of these features on a single attribute map display, we have developed the multilevel composition technique. It is an innovative and robust 5-step technique involving RGB blending of multilevel amplitude maps (Figure 3a). The technique involves selecting a particular time or depth window/interval of interest within a preconditioned seismic image. The optimal window should contain high amplitude features of geological interest to the interpreter. This is followed by the selection and interpretation of one or more horizons near the chosen window for attribute computations (Figure 3b). The most preferable horizons are generally continuous and close to the geological features of interest. The selected window is then divided into 3 sub-windows to enable detailed interval by interval characterization of the features within the window. Amplitude-accentuating attributes are subsequently computed for each sub-window using the interpreted horizon as a reference. This is followed by color assignment in which the resulting attribute maps are assigned to red, green, and blue colors and are co-rendered in the RGB color space (Figure 3b-d). The color assignment performed in this technique is similar to that employed in spectral decomposition procedure, where the color assignment is frequency dependent. However, unlike spectral decomposition, the colors here are assigned based on the stratigraphic position of the geological features of interest i.e., depth dependent rather than frequency-band dependent. When certain features of interest are best displayed in a particular secondary color, the interpreter can use a color assignment order that will enhance those features.

Figure 3a presents a sample outline/workflow of the multilevel composition technique. The interval of interest is 15-120 m below the seafloor (Figure 3a). This interval was determined by measuring the separation between the top and bottom of the window where the features of interest dominantly occur. However, identifying a continuous and easy-to-interpret horizon for attribute computation at this interval seems difficult. The seafloor horizon (at 0 m) was subsequently chosen because it is continuous, easy to interpret and lies near the interval. This was followed by the division of the interval into three sub-intervals/sub-windows i.e. 15-30 m, 25-60 m and 55-120 m based on the predominant vertical sizes of the features of interest within the window (Figure 3b). The first digits of each sub-window represent its upper limit, while the last digits represent its lower limit. Using the interpreted horizon (seafloor) as reference, the signal envelope attribute was computed for the three sub-windows (Figure 3c). This was followed by color assignment in which the resulting attribute maps were assigned to red (shallowest; 15-30 m), green (intermediate; 25-60 m), and blue (deepest; 55-120 m) colors (Figures 3b-c). It should be noted that the overlap in the selection of sub-windows was done to allow for intermixing of colors. Following color assignment, the maps are co-rendered and displayed in the RGB color space to obtain an enhanced view of subsurface elements (Figure 3d). For effective RGB blending of computed attribute maps, such as the one in Figure 3c-d, the colors should be balanced by ensuring that the amplitude responses at the different windows do not mask themselves.

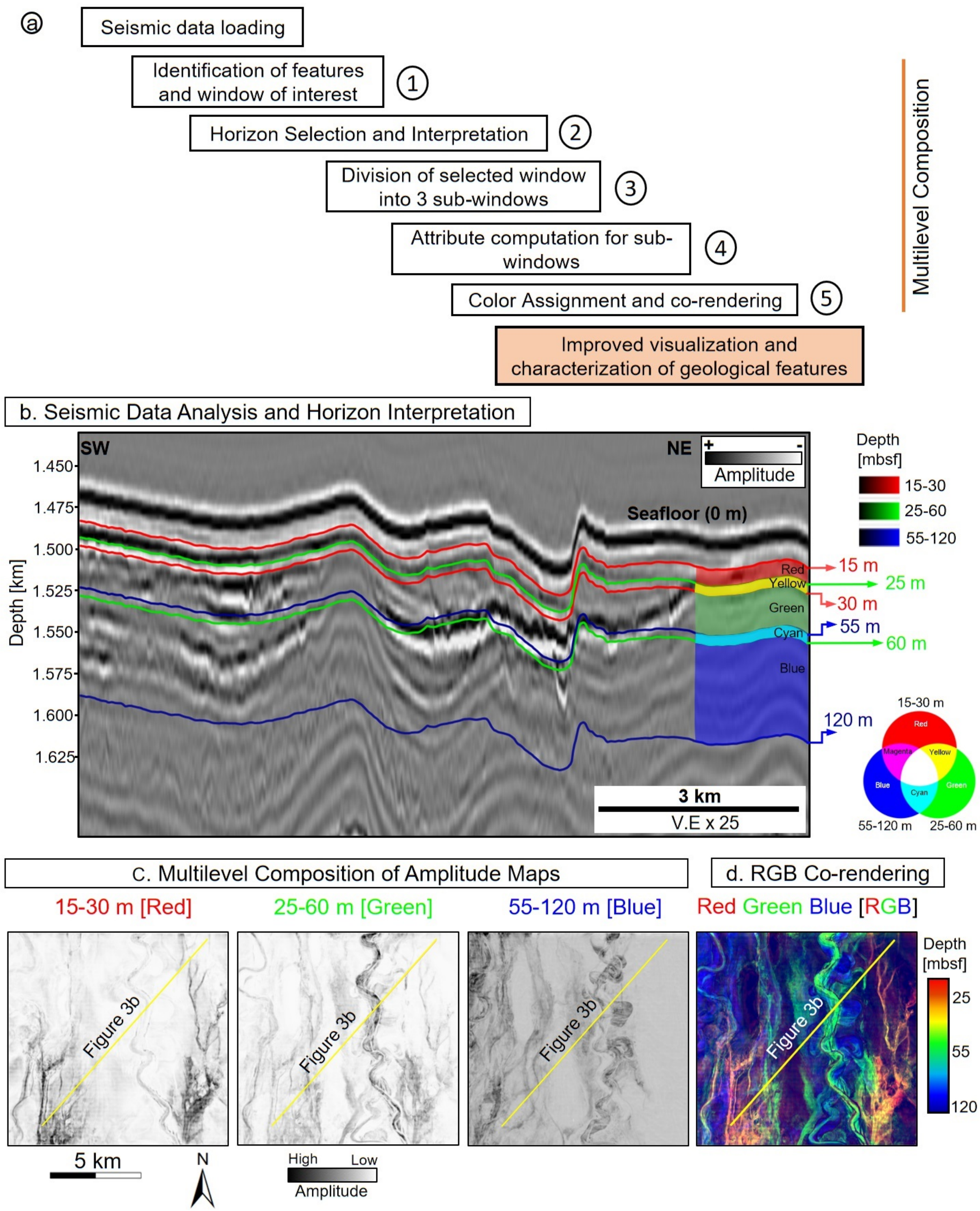

Figure 3. (a) The multilevel composition technique workflow. (b) A seismic profile from the Sara-Mira 3D seismic dataset (Figure 1 and Table 1), demonstrating the attribute extraction

procedure. Here the seafloor is used as a single reference surface. The depth interval of geological interest (15-120 m below the seafloor) is divided onto three sub-windows: 15-30 m (bounded by red lines), 25-60 m (green lines) and 55-120 m (blue lines). Attributes extracted in each of these intervals are assigned with red, green and blue colors, while additional colors result from blending of these basic color layers (as schematically highlighted on the right). (c) Signal envelope attribute maps extracted for each of the three depth intervals shown in (b), each highlighting different geological features. (d) Blending of the signal envelope maps in the RGB color space, with the attribute maps assigned the red (shallowest; 15-30 m), green (intermediate; 25-60 m), and blue (deepest; 55-120 m) colors. The combined color scale (left) estimates the depth below the seafloor represented by each of the blended image colors. The profile in (b) is outlined (yellow line) in (c) and (d).

3.4 Spectral decomposition

Spectral decomposition (Partyka et al., 1999) was performed with reference to the seafloor horizon and was done within the interval of interest in this study, using central frequencies of 15 Hz, 30 Hz, and 70 Hz. This was followed by color blending in the RGB color space (Figure S1b). The spectral decomposition was carried out in this study to enable comparison of its results to those derived from the multilevel composition technique and to verify the consistency between the two complementary techniques.

4. Case study applications of Multilevel Composition

4.1 Eastern deep-sea fan of the Nile, eastern Mediterranean

The first case study area is in the eastern extension of the deep-sea fan of the Nile in the Levant Basin, eastern Mediterranean (Figure 1a). The interval of interest in this area is of the Quaternary period. It is dominated by multiple Nile-derived channels, levee and lobe shape-based features that are buried within multiple intervals below the seafloor and interact with fold ridges (Clark and Cartwright, 2009; Folkman and Mart, 2008; Sagy et al., 2020; Tayber et al., 2019). The goal of the RGB-based multilevel composition technique is to better visualize and characterize these depositional elements and to resolve their complexities. It enables better understanding of the sediment deposition patterns and provides an important approach to limit interpretation time in this area. In the evaluation of the seismic dataset from this area, the geological features of interest in this study are located within 15-120 m below the seafloor. This window was further divided into three sub-windows 15-30 m, 25-60 m, and 55-120 m, based on the distribution of the high amplitude features within the intervals (Figure 3). The subsequent steps of the proposed method are detailed in the data and methodology section.

4.1.1 Background geology

The Levant Basin was developed following the opening of the Neo-Tethys Ocean (Garfunkel, 2004), the formation of deep marine basinal structure in the Early Mesozoic, and the Late Cretaceous convergence of Early Mesozoic structures (Gardosh and Druckman, 2006). During the Oligocene a system of submarine canyons along the Levant margin had developed, supporting sediment transport to the deep-basin (Buchbinder and Zilberman, 1997; Druckman et al., 1995). This was followed by a restriction in the connection between the Mediterranean Sea and the Atlantic Ocean in the Messinian, leading to the deposition of up to 2 km thick evaporites (Meilijson et al., 2019; Roveri et al., 2014). The evaporites are overlain by 1-2 km thick northwest prograding mainly Nile-derived Pliocene to Quaternary marine siliciclastics and claystones (Buchbinder and Zilberman, 1997; Frey-Martínez et al., 2006; Sagy et al., 2020; Schattner and Lazar, 2016). The accumulation of sizeable volumes of coarse sediments in the Pliocene (Niyazi et al., 2018; Sagy et al., 2020; Zucker et al., 2021) and the formation of the present-day Nile resulted in a large sedimentary cone that is >8km thick (Macgregor, 2012) and associated with several channel systems which stretch northward as far as the Herodotus and Levant Basins (Folkman and Mart, 2008).

In the Levant margin, sediment depositions in the Quaternary resulted in the accumulation of ~1km thick Nile-derived sediments. The sediments thin towards the continental rise and deep basin, where they vary between a few tens and a few hundreds of meters (Ben-Gai et al., 2005; Ben-Zeev and Gvirtzman, 2020; Sagy et al., 2020; Schattner et al., 2017). Sediment transport in the basin margin was facilitated by counterclockwise northward prevailing currents and waves (Özsoy et al., 1993; Reiche et al., 2018; Schattner and Lazar, 2016). The Quaternary in the Levant was also associated with the deposition of sediments via channel systems. These sediments are buried within the uppermost ~200 to 250 m below the seafloor in the Nile fan, the eastern flank of which extends into the Levant Basin (Ben-Zeev and Gvirtzman, 2020; Sagy et al., 2020; Tayber et al., 2019). The sediments occur within multiple intervals (Tayber et al., 2019), are deposited within a northeast-southwest (NE-SW)-oriented depocenter in the deep basin, and pinch out on the present-day continental shelf (Sagy et al., 2020). Downslope sediment flows and landslides, such as those in the eastern Levant margin (Eruteya et al., 2016; Frey-Martinez et al., 2005; Gadol et al., 2019; Katz et al., 2015) are secondary sources of sediments, complementing Nile-derived sediment supply to the deep basin. Increasing load of Plio-Quaternary sediments above the Messinian salts combined with northward push of sediments by the Nile cone triggered mobilization of the Messinian salts. This mobilization promoted widespread deformation of the overlying sediments across the eastern Mediterranean since the Pliocene (Ben-Zeev and Gvirtzman, 2020; Bertoni and Cartwright, 2006; Cartwright et al., 2012; Gvirtzman et al., 2017; Zucker et al., 2020). In the Levant Basin, this deformation is recorded in the form of several fold ridges and faults, many of which are observed on the present-day seafloor, where they interact with deep-sea channels (Clark and Cartwright, 2009; Gvirtzman et al., 2015; Zucker et al., 2017).

Figure 4. (a) Bathymetry of the case study area in the eastern Nile fan in the Levant Basin, as picked from the Sara-Mira 3D seismic dataset, color-coded with water depth (right color bar) and shaded based on the bathymetric gradient. (b) A multilevel RGB composite image of signal-envelope maps, extracted from the Sara-Mira 3D seismic dataset for the 15-30 m (red), 25-60 m (green), and 55-120 m (blue) below the seafloor (bottom color coding). The middle color bar estimates the depth below the seafloor, which is reflected by the combined colors of the image. The image delineates the relative stratigraphic position of buried paleo- deep-water channels and splays and their interactions, and helps to constrain the evolution of this system. (c) An RGB composite image of spectral decomposition results over the same 15 to 120 m interval below the seafloor, combining the 15 Hz (red), 35 Hz (green), and 70 Hz (blue) central frequency bands (color coding on the right). This image delineates the same features as in (a), color coded in relation primarily to their thickness. (d) An W-E oriented seismic profile (white outline in a-c) showing a band of discontinuous, multilevel high amplitude sub-seafloor seismic reflectivity down to ~1.5 below the seafloor, and which pinches-out at ridge flanks in the east and west. This reflectivity is imaged in (b) and (c) as the intricate system of buried deep-water channels and related features.

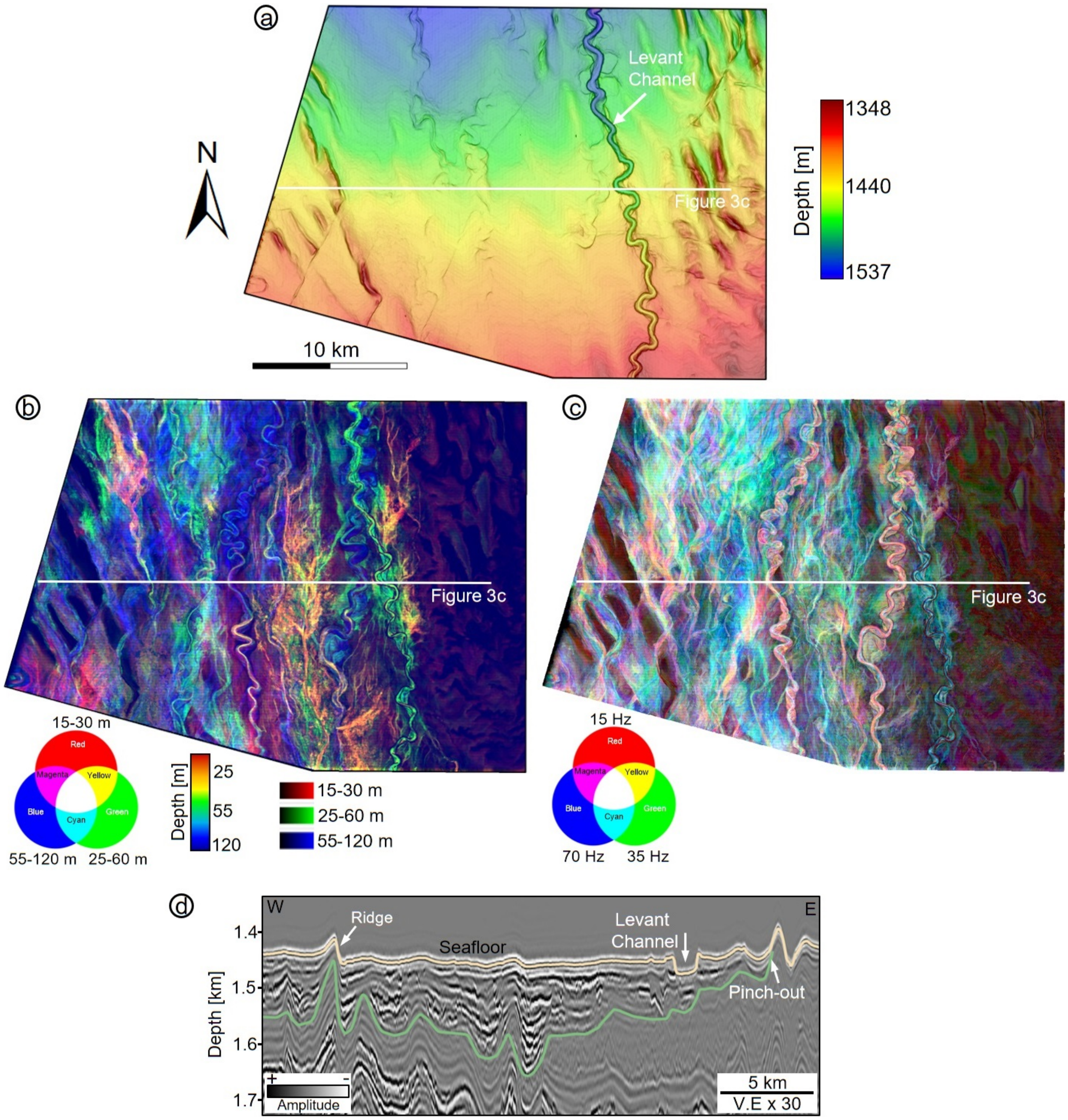

4.1.2 Multilevel composition of buried deep sea channel systems

The bathymetry of the study area comprises (a) NNW-SSE trending ridges that are prominent in the western and eastern parts of the study area and are deformed by lineaments with varying orientations (Figure 4a). The ridges are suggested to belong to the larger circum-Nile deformation belt (Gvirtzman et al., 2015), which formed following shortening that resulted from the out-squeezing of salts from the Nile delta towards the NNE (Cartwright and Jackson, 2008; Netzeband et al., 2006). (b) A NNW-SSE oriented deep-water channel system, with a prominent sinuous seafloor channel, the Levant channel (Gvirtzman et al., 2015), extending across the center of the entire study area from south to north. This channel is ~34 km long within the study area, is 300 to 500 m wide and is ~30 m deep with respect to the surrounding. The marks of several additional, apparently abandoned and partly buried, channel elements are apparent around and to the west of it (Figure 4a).

Following the multilevel composition (Figure 4b), a multitude of older channels, lobes and splays are revealed to make up the sedimentary fill, around the prominent ridges (dark) in the western and central parts of the study area. These features are characterized by red, green, and blue colors and their derivatives, which denote shallow (15-30 m) to deep (55-120 m) occurrence of the paleo-depositional features within the dataset, respectively. Conversely, a shut-off of composed amplitude, marking the absence of channels systems, characterize the easternmost part of the study area, near the base of the southeastern continental margin of the Levant (Figure 4b). The full wealth of paleo-depositional features is also observed on a spectral decomposition image (e.g., Partyka et al., 1999) of the same interval (Figure 4c). However, in this case color coding represents the frequency content of the seismic signal, which is associated with different thicknesses of the depositional features imaged. A comparison of Figures 4b and 4c demonstrates the complementary utility of the commonly used spectral decomposition and our new multilevel composition maps.

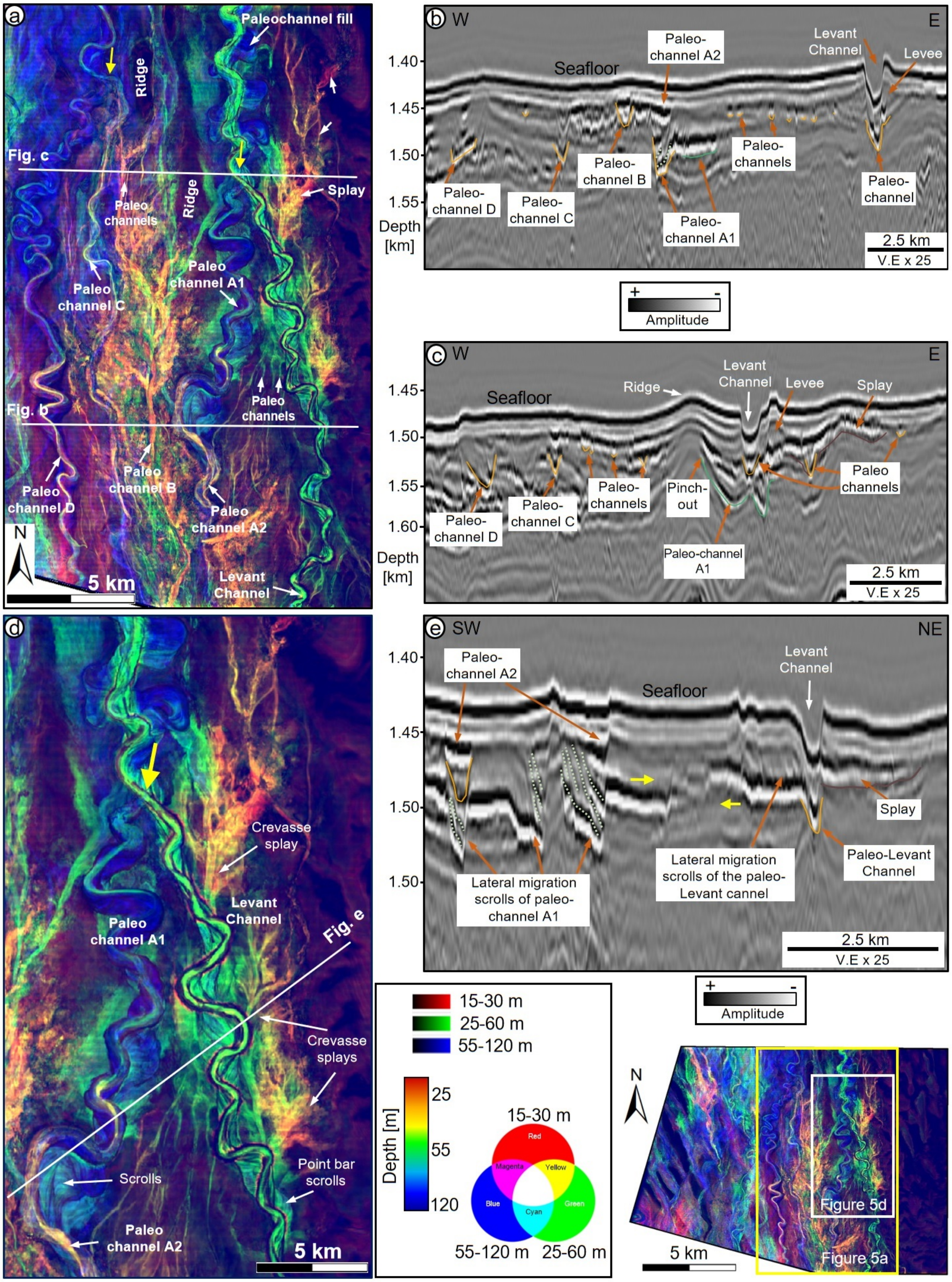
a
Paleochannel fill
Ridge
Fig. c
Splay
Paleo channels
Ridge
Paleo channel A1
Paleo channel C
Paleo channels
Fig. b
Paleo channel B
Paleo channel D
Paleo channel A2
N
5 km
Levant Channel
b W
E
Seafloor
Paleo-channel A2
Levant Channel
Levee
Paleo-channel D
Paleo-channel C
Paleo-channel B
Paleo-channel A1
Paleo-channels
Paleo-channel
Depth [km]
2.5 km
V.E x 25
Amplitude
c W
E
Seafloor
Ridge
Levant Channel
Levee
Splay
Paleo-channel D
Paleo-channel C
Paleo-channels
Pinch-out
Paleo-channel A1
Paleo channels
d
Crevasse splay
Levant Channel
Paleo channel A1
Fig. e
Crevasse splays
Scrolls
Point bar scrolls
Paleo channel A2
5 km
e SW
NE
Paleo-channel A2
Seafloor
Levant Channel
Splay
Paleo-Levant Channel
Lateral migration scrolls of paleo-channel A1
Lateral migration scrolls of the paleo-Levant cannel
15-30 m
25-60 m
55-120 m
Depth [m]
Red
Magenta
Yellow
Blue
Cyan
Green
55-120 m
25-60 m
Figure 5d
Figure 5a

Figure 5. (a) A zoomed part of Figure 4b RGB multilevel composite map (see bottom right for the location and color scales), highlighting multiple buried paleo depositional features (e.g. as labeled) within the study area. The colors of the different features represents their relative stratigraphic positions. (b, c) W-E oriented seismic profiles from the Sara-Mira 3D seismic dataset (outlined in white in (a)), show the different depositional elements highlighted by the multilevel composition in (a) in their stratigraphic context. (d) A zoomed part of (a) (see bottom right for the location and color scales) showing that the stratigraphically higher (green colored) paleo Levant channel overlaps northwards (yellow arrow) onto the track of the stratigraphically lower (blue colored) paleo channel A1. Paleo channel A2 is etched into the overburden overlaying paleo channel A1, and is stratigraphically higher than both, Note the occurrence of several scrolls indicating lateral migration of the channels. (e) A SW-NE-oriented seismic profile (outlined in white in (d)) shows the different depositional elements highlighted by the multilevel composition in (d) and demonstrates the difficult in interpreting the relative stratigraphic positions of paleo channel A1 and the paleo Levant channel, a difficulty which is resolved by the multilevel composition in (d).

A seismic profile across the study area reveals that the paleo-depositional features mapped by the multilevel composition are imaged as pervasive, multilevel and discontinuous high amplitude band of reflections (Figure 4d). These reflections pinch-out at ridge flanks in the eastern part, where they are replaced by more continuous, smooth and dominantly low amplitude reflections (Figure 4d). The low amplitude reflections manifest the shut-off of composed amplitude in the eastern part (Figure 4b). Several previous studies have suggested that sediment supply to the deep-basin in the Quaternary is mainly by Nile-derived deep-water channels and lobes (Folkman and Mart, 2008; Tayber et al., 2019; Kanari et al., 2020; Sagy et al., 2020). Sediment supply in the basin margin is by alongshore transport, followed by sediment descent along the continental slope and rise (Schattner and Lazar, 2016). Consequently, it is suggested that the marked variation in the composed amplitude response between the two areas i.e. occurrence of channels and splays across multiple depths in the west and their absence in the eastern part, evidences the primary differences in sedimentation patterns in the area in the later part of the Quaternary.

The paleo-depositional features in the central to western part of the study area are the focus of this section and are investigated in detail in subsequent paragraphs. Multilevel composition (Figure 5a) delineates between the paleo-Levant Channel, paleo-channels A-D, and several smaller paleo-channels. Evidence for the occurrence of the paleo-Levant Channel is that an older channel, similar to the present-day Levant Channel, is observed at its location (Figure 4a-b and 5). On seismic reflection profiles, the paleo-channels are characterized by U- or V-shaped depressions and low to high amplitude infills (Figure 5b-c). The low to high amplitude infills could indicate lithology changes, for instance, sand- and mud-bearing lithologies, respectively (Posamentier, 2003). In addition, the paleo-Levant Channel is associated with a dominant green color on the multilevel composed amplitude map, which indicates that it extends stratigraphically between 25-60 m below the seafloor, i.e. at an intermediate stratigraphic level within the interval of interest. Complementing this detail are minor color variations, which seem to correspond with changes in the internal character of the channel on the spectral decomposition image (Figure 4c and Supplementary Figure 1). On the seismic reflection data, the present-day Levant Channel is characterized by low amplitude reflections that reduce in thickness on its two sides (Figure 5b), likely indicating mud-prone levees (Posamentier, 2003).

The paleo-Levant Channel and paleo-channels A and D display evidence of intense avulsion, indicated by multiple meander scrolls below the channels on the multilevel composed amplitude map and bent reflections on seismic data (Figure 5a, b, d, and e) i.e. lateral migration and vertical aggradation (Kolla et al., 2007; Posamentier and Kolla, 2003). In addition, the paleo-Levant Channel and paleo-channels A and D have high sinuosity, while paleo-channels B and C have low sinuosity. Increase in sinuosity is observed in the northern part of paleo-channel C (Figures 4b-c and 5a and d). Since the paleo-seafloor was mainly shaped by salt-deformation-related ridges, the substantially similar sinuosity of most of the paleo-channels may be partly due to their response to slope gradient and confinement changes (Clark et al., 1992; Peakall et al., 2012). This may also be due to an overall low energy and muddy flow into the study area from the Nile cone, as sinuous channels are generally linked to low energy muddier flow (Janocko et al., 2013).

The multilevel composition shows remarkable interaction between paleo-channels as the paleo-Levant Channel (green) is seen to merge with or cross the path of the older (blue) paleo-channel A in its northern portion (yellow arrows in Figure 5a and d). As the channels cross, the paleo-Levant Channel (green) assumes the flow path of paleo-channel A and incises into its underlying fill (blue). In the context of this study, features coded in blue color are the deepest and presumably the oldest stratigraphic features, while green coded features are within intermediate depth. Paleo-channel A fills are identified as high amplitude seismic reflections below the Levant Channel on seismic reflection data (Figure 5c). Similarly, paleo-channels C and D are observed to merge in the northern section of the study area (Figure 5a). Consequently, the multilevel composition technique adequately delineates the strong interaction between these multi-depth paleo-channels. The merger of these channels is also visible on the spectral decomposition image, which highlights the differences in the internal character of these features rather than their relative position (Figure 4c). The channel merging or crossing relationship is not limited to the study area.

Kanari et al. (2020) has suggested that the Levant Channel alone crosses the path of about ten different older channels as it meanders up north within the eastern Nile fan in the Levant Basin.

Furthermore, multilevel composition (Figure 5a and d) reveals several dendritic and small channels up north of paleo-channel B and between the paleo-Levant Channel and paleo-channel A. The later set of small channels are directed north-eastward, where they extend northwards towards deposits that spill-out from a bend along the Levant Channel. Similar spill-out or off-flank deposits are also identified in the northern section of the Levant Channel, where they are associated with several north-oriented dendritic channels. These deposits are predominantly characterized by a mixture of red and yellow colors on the composed amplitude map (Figure 5a and 5d). The yellow color is an intermix of red (15-30 m below the seafloor) and green (25-60 m below the seafloor) colors, representing the presence of these features about 25 to 30 m below the seafloor. The features characterized by the red color are the shallowest, and possibly youngest stratigraphic features, or possibly associated with lower overburden accumulation rates.

In addition, the spill-out deposits are characterized by continuous to jagged or serrated high amplitude reflections with associated V-shaped depressions on seismic reflection profile (Figure 5b). Based on their appearance on the multilevel composed amplitude map and seismic profile, the deposits are interpreted as crevasse splays (Burns et al., 2017; Gulliford et al., 2014), while the jagged reflections represent small channels within them i.e. a sort of distributary channel network. The crevasse splay deposits may be related to the spill-out and deposition of sediments over the bank of the Levant Channel. This could happen as flow breached the less competent levee, acting as the confining wall of the channel, during periods of enhanced flow from the Nile system into the study area. In general, the occurrence of channels and splays within the study area may reflect a period of elevated sediment supply. This is possibly in response to enhanced Nile-derived sediment flux into the Levant Basin in parts of the Quaternary (Ben-Gai et al., 2005; Sagy et al., 2020).

In terms of ridge-flow interactions, multilevel composition reveal that the paleo-depositional features generally deviate away from the ridges (Figures 4b and 5a). The features are observed as reflections pinching-out towards ridge flanks on seismic reflection data (Figure 5c). This may be caused by the increase in paleo elevation as the depositional elements approach the ridges, which were already areas of positive seafloor topography. It is observed from the multilevel composed amplitude map (Figure 5a) and on a seismic profile (Figure 5c) that the occurrence of the ridges caused facies to migrate towards topographic lows. Consequently, observations from multilevel composition reveal inherited topography dictates the localization of flow and sedimentation in topographic lows in the study area. Flow diversion by ridges as shown via multilevel composition in the study area seems to be occurring over a large part of the Levant Basin as similar relationships have been shown from deeper parts of Nile fan in the Levant Basin (Clark and Cartwright, 2009; Zucker et al., 2017). Similar interactions have also been identified from other geological settings, such as the Niger Delta, where there is an interplay between shale tectonics-driven ridges and sedimentation (Jolly et al., 2016).

Overall, our analysis, using the multilevel composed amplitude map of the study interval, reveals that the study area is characterized by paleo-depositional features, most of which occur across multiple intervals. This could indicate the features belong to different evolutionary phases. Consequently, the multilevel composition technique (Figures 4b and 5a and d) is able to reveal meaningful color-coded depth information, which provide novel additions towards understanding the evolution of the depositional features. In general, multilevel composition reveals that Nile-derived sediments are deposited in the study area by two dominant flow types; (a) confined flow via predominant high sinuosity channel systems and (b) unconfined flow via crevasse splays.

4.2 Omakere Ridge, Hikurangi Margin, New Zealand

The second case study area is in the Omakere Ridge in the Hikurangi Margin, New Zealand (Figure 1b). Verified seep sites including the Kea, Kaka, Kakapo, Moa and Bear's Paw (Figure 6) and their faunal assemblages constitute extensive evidence of active microbial methane discharge at the ridge. Additional evidence of seepage include several authigenic carbonate slabs at the seeps and gas hydrate recovered below the Bear's Paw site (Barnes et al., 2010; Faure et al., 2010; Greinert et al., 2010; Jones et al., 2010). Migrating fluids within the Omakere Ridge are generally channeled from deep, biogenic sources into the hydrate zone before eventually escaping at seafloor sites (Plaza-Faverola et al., 2014; Watson et al., 2020). The goal of the multilevel composition technique here was to illuminate the seeps, determine their full extent and better constrain their links to underlying potentially gas-bearing intervals. In the evaluation of the Omakere 3D seismic dataset, acquired in this area, it was determined that the anomalous seismic responses directly connected with the seafloor (0 ms) seeps are within up to 40 ms below the seafloor. An investigation of the vertical distribution of these features revealed that it would be useful to use the seafloor as the reference horizon and consider the intervals 0-5 ms, 4-15 ms and 12-40 ms below it. The maximum positive amplitudes for the three windows were extracted and were subsequently blended in the RGB color space (Figure 7). To reveal the connection between the seafloor seeps and sub-surface gas-bearing intervals, three reference horizons: A1, A2 and A3 were identified, following Plaza-Faverola et al. (2014), and mapped across the dataset. The RMS amplitude maps of these horizons were computed and selectively co-rendered with selected maximum amplitude maps from the three shallow sub-windows (Figures 7, 9 and 10).

4.2.1 Background geology

The Hikurangi margin is an extensive gas hydrate province (Pecher et al., 2010) and a component of the active Kermadec-Hikurangi subduction zone situated at the boundary where the Pacific Plate subducts westward and obliquely beneath the Australian Plate at about 40–50 mm/yr (Figure 1b; Beavan et al., 2002). At this margin, a component of the margin-parallel motion is being accommodated by strike-slip faulting (Collot et al., 1996; Nicol et al., 2007) as relative plate motion becomes more oblique southward (Wallace et al., 2012). The tectonic style of the Hikurangi Margin is determined by certain factors such as thickness and roughness of the underthrusting crust, obliquity of convergence, and thickness of subducting sediments (Barnes et al., 2010; Collot et al., 1996). The Omakere Ridge is located in the central part of the Hikurangi margin, a region that is predominantly dominated by accretion (Jones et al., 2010) and characterized by many prominent, NE-SW oriented slope parallel anticlinal ridges, one of which is the Omakere Ridge. The ridge has a relief of ~500 m in water depth of 1100 to 1200 m (Barnes et al., 2010) and a surface that is largely marked by landslides, which are particularly frequent along its steep forelimb flank (Barnes et al., 2010).

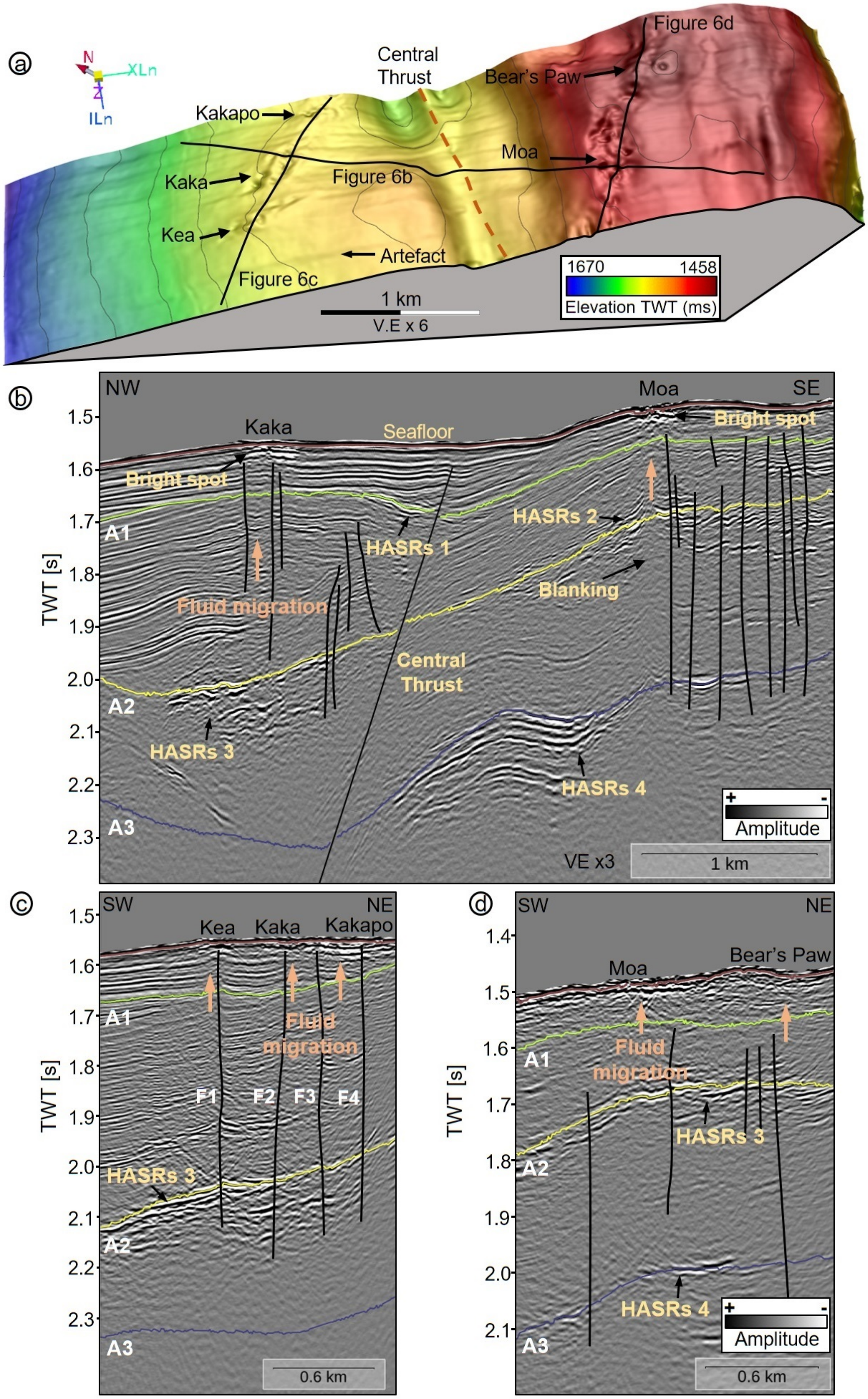
a
N
XLn
ILn
Central Thrust
Figure 6d
Bear's Paw
Kakapo
Moa
Kaka
Figure 6b
Kea
Artefact
Figure 6c
1 km
V.E x 6
1670
1458
Elevation TWT (ms)
b
NW
Moa
SE
Kaka
Seafloor
Bright spot
Bright spot
A1
HASRs 1
HASRs 2
Fluid migration
Blanking
Central Thrust
A2
HASRs 3
HASRs 4
A3
TWT [s]
Amplitude
VE x3
1 km
c
SW
NE
Kea
Kaka
Kakapo
A1
Fluid migration
F1
F2
F3
F4
HASRs 3
A2
A3
0.6 km
d
SW
NE
Moa
Bear's Paw
A1
Fluid migration
HASRs 3
A2
HASRs 4
A3
Amplitude
0.6 km

508

Figure 6. (a) A 3D shaded relief depiction of the Omakere Ridge bathymetry (color coded by water depth), as mapped based on the Omakere 3D seismic dataset, showing two ridges separated by a trench that marks the surface projection of the central thrust fault. The morphological expressions of the Kea, Kaka and Kakapo seeps appear to the west of the central thrust fault and the Moa and Bear's Paw seeps to the east of the thrust. Black lines highlight the seismic profiles shown in (b)-(d). (b) A NW-SE seismic profile from the the Omakere 3D seismic dataset, crossing the Kaka and Moa seafloor seeps and showing their underlying features. Three reference horizons, A1, A2 and A3, mapped across the dataset following Plaza-Faverola et al. (2014) are maked in green, yellow and blue, respectively. We note that these horizons may not represent the same stratigraphic level of the two sides of the central thrust fault (black line). Also shown are localized subsurface high amplitude reflections (HASRs 1-4), sub-seep bright spots with associated underlying vertical zone of blanked seismic reflections, and a set of minor faults (black lines). (c) A NE-SW seismic profile from the Omakere 3D seismic dataset across the Kea, Kaka and kakapo seeps, showing their underlying enhanced reflections and faults (F1-F4). (d) A seismic profile from the Omakere 3D seismic dataset across the Moa and Bear's Paw seeps, showing their undelaying HASRs and faults. Peach arrows indicate potential sub-vertical fluid focusing from the HASRs to the seafloor seeps. TWT[s]: Two-Way Time in Seconds.

The Omakere Ridge is associated with a variable subsurface structure that is linked to major thrust faults. Underlying the easternmost flank of the Omakere Ridge is a system of active thrust and deeper inactive thrust imbricate (Barnes et al., 2010). These structures are complemented by another active thrust splay that reaches the seafloor around the center of the ridge i.e. the ''central thrust'' (Plaza-Faverola et al., 2014). The ridge is underlain by a wedge of Cretaceous and Paleogene rocks that underlie folded Miocene to Recent sediments in the hanging wall of the lower thrust faults. Several active seeps, including the Kea, Kaka and Kakapo (Faure et al., 2010; Greinert et al., 2010; Jones et al., 2010) lie in the hanging wall of the central thrust, while the Bear's Paw and Moa seeps lie in the footwall of the thrust. The seeps were suggested by Plaza-Faverola et al. (2014) to be linked to deeper gas-bearing intervals through several complex fault systems, which serve as migration routes.

4.2.2 Observations from Seismic reflection data

The seafloor seeps in the study area are associated with five elongate seafloor depressions, which represent the Kea, Kaka, Kakapo, Moa and Bear's Paw cold seeps (Figure 6a). The Kakapo, Kaka, and Kea seeps are individually oriented NNW-SSE and collectively E-W-oriented, while the Bear's Paw and Moa seeps are ENE-WSW oriented. Seeps within the Omakere Ridge are associated with underlying localized high amplitude seismic reflection (HASR) anomalies or bright spots (Figure 6b-d). The anomalies are linked to underlying zones of vertically blanked reflections on seismic reflection profiles. A set of faults: F1-F4 are observed below the Kea, Kaka and Kakapo seeps (Figure 6c), extending between deeper HASRs (1-4) to shallower intervals below the seafloor seeps. The shallowest, HASRs 1 is identified in proximity of horizon A1, within 0.1 second of the seafloor (Figure 6b). Seismic reflections representing HASRs 2 are faulted and located at about 0.2 second beneath the Moa and Bear's Paw seep sites (Figure 6b). Similarly, HASRs 3 is faulted and observed below the Kaka, Kea and Kakapo seep sites. HASRs 3 appears to be connected to shallower intervals below the seeps by faults F1-F4. HASRs 4 is folded and faulted, and represents the deepest of the HASRs analyzed in the study area (Figure 6b). HASRs 1-4 are have been suggested by Plaza-Faverola et al. (2014) to manifest fluid-bearing sediments. In addition, localized sub-seep HASRs or bright spots are identified on the amplitude maps extracted from 0-5 ms, 4-15 ms and 12-40 ms below the seafloor (Figure 7a-c). An additional near seafloor localized HASR anomaly is observed ~0.1 km west of the Bear's Paw seep site.

4.2.3 Multilevel composition of the seafloor seeps and deeper gas-bearing intervals

Multilevel composition of amplitude maps computed at sub-windows below the seafloor adequately illuminates the five seep sites as localized high amplitude zones with varying colors and intensities (Figure 7d). While the composed amplitude at the Kea, Kaka and Kakapo seep sites are mutually distinguishable, the composed amplitude at the Bear's Paw and Moa sites appear continuous, revealing a significant interlink between the two seep sites. Clearly delineated by the multilevel composition technique, this linkage was first suggested by Jones et al. (2010) based on sidescan sonar imaging. Additionally, the multilevel composition reveals a larger extent and intensity of deeper reflectivity (at ~20 ms; cyan) beneath the northern part of Moa, and shallower and lower intensity reflectivity beneath the southern part of Moa and Bear's Pow. Together the mutual interlink and relative depths may suggest lateral flow of gas in the shallow subsurface from the northern part of Moa southwards and northwards. The areas of the seeps is estimated based on their multilevel composed amplitude responses (Figure 7d) at ~0.11 km^2 for Kea, ~0.17 km^2 for Kaka, ~0.18 km^2 for Kakapo and ~0.5 km^2 for Moa and Bear's Paw. The main part of the Bear's Paw site has an area of ~0.18 km^2 (Figure 7d).

In addition, at ~0.1km to the west of the Bear's Paw is an additional multilevel composed amplitude anomaly with an area of ~0.07 km^2 (Figure 7d). Seismic reflection data (Figure 8) reveal that it is associated with a seafloor depression and underlying localized HASRs, which are linked to similar HASRs below the Bear's Paw. It is also underlain by faults that reach HASRs 3 at depth, extend upwards and terminate in shallow sediments below the seafloor anomaly (Figure 8). These observations suggest the feature is either an extension of the Bear's Paw seep or another distinct seep site that was not previously discovered. The absence of any significant linkage between this suspected seep and the Bear's Paw, at least in their multilevel composed amplitude responses, supports the later interpretation.

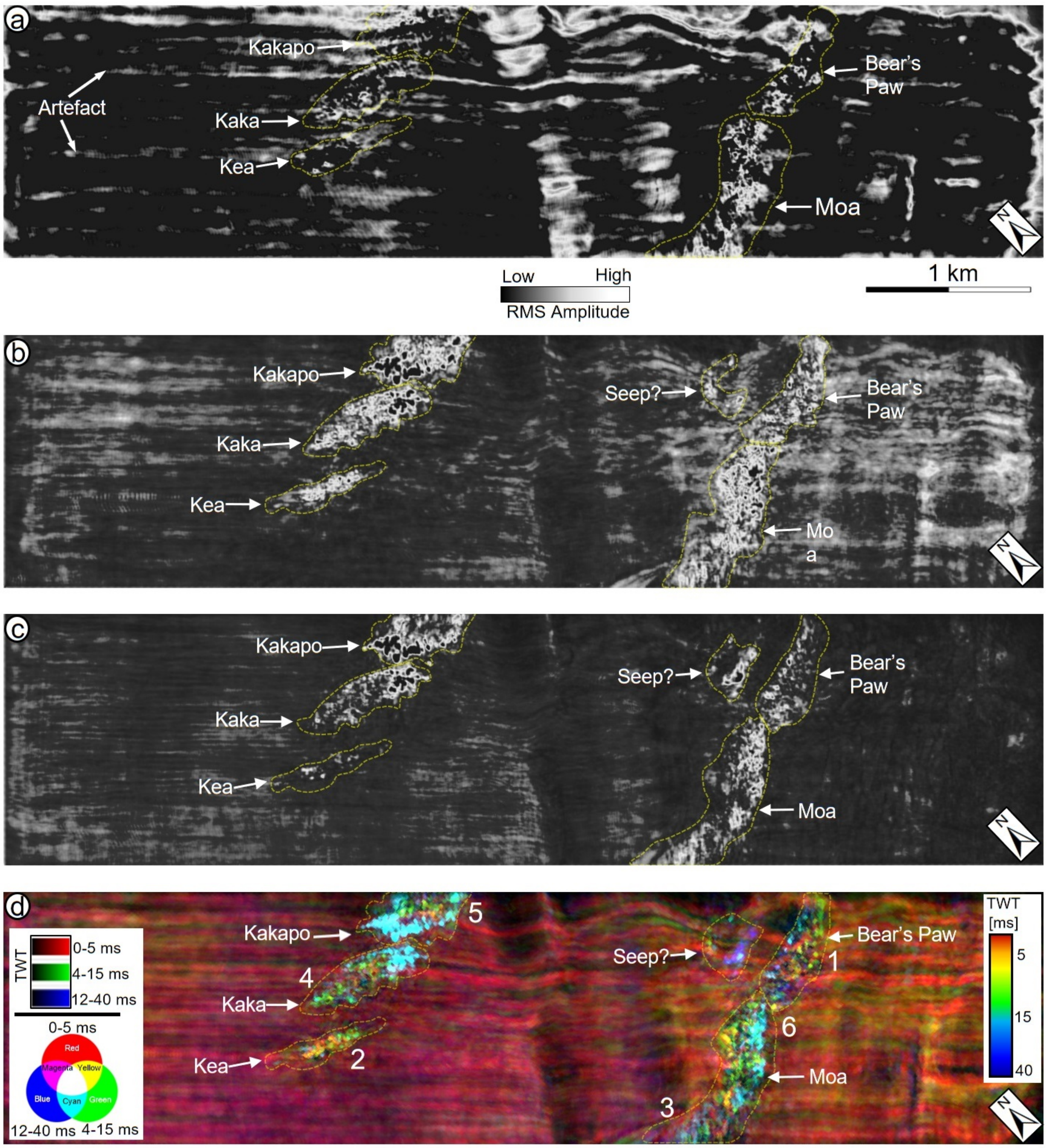

Figure 7. (a) A maximum positive amplitude map, extracted at 0-5 ms of the seafloor from the Omakere 3D seismic dataset, revealing localized high amplitude anomalies at the locations of the Kea, Kaka, Kakapo, Moa and Bear's Paw seeps, as well as striped acquisition artefacts. (b) A maximum positive amplitude map, extracted at 4-15 ms below the seafloor, highlighting localized amplitude anomalies below the seafloor seeps. Note the additional localized amplitude anomaly to the north of Bear's Paw seep. (c) A maximum positive amplitude map, extracted at 12-40 ms below the seafloor, also showing localized amplitude anomalies at the location of the seeps. Note the reduced amplitude responses at the Kea seep and the enhanced response north of the Bear's Paw site. (d) A multilevel RGB composite of the amplitude maps at (a) (0-5 ms, red), (b))(4-15 ms, green), and (c) (12-40 ms, blue), highlighting the throughout amplitude enhancement at the seeps (bright colors) and the different depth of their feeding systems (green and blue tones), as well as illuminating the anomaly to the north of the Bear's Paw seep. Numbers rank the intensity of each of the seeps (1-highest and 6-lowest) based on seafloor observations by Jones et al. (2010), which appear to be inverse of the intensities of their composed amplitude responses. Note the color scale in Figure 7d. TWT [ms]: Two-Way time in milliseconds.

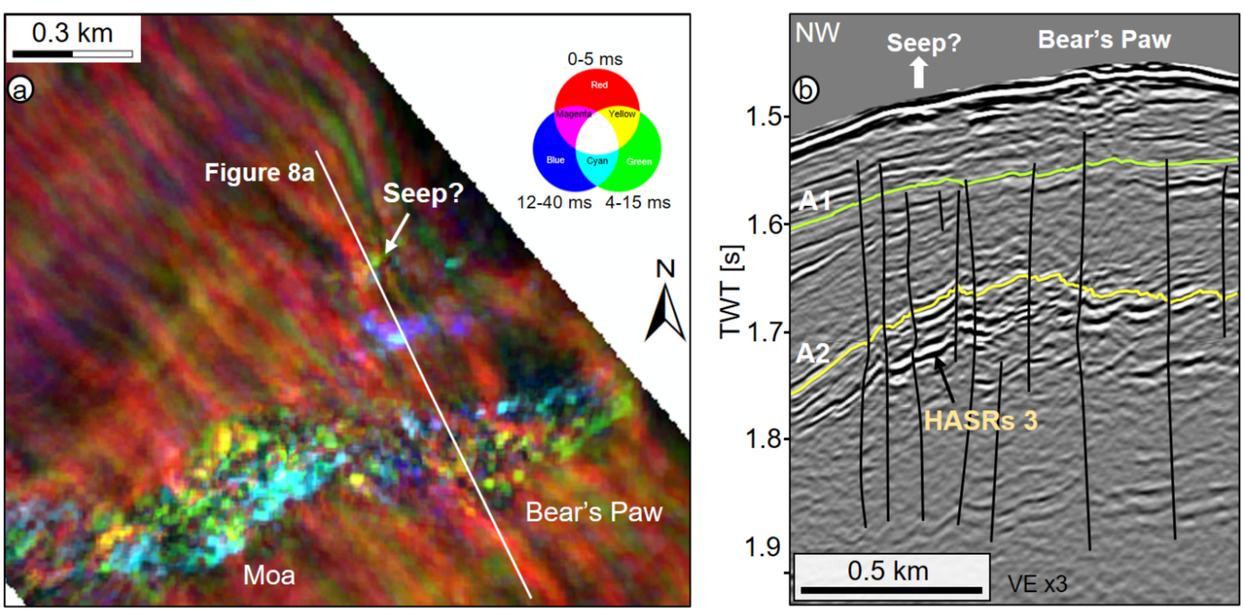

Figure 8. (a) A zoomed part of the multilevel RGB composite of Figure 7d, covering the vicinity of Bear's Pow and Moa seeps. (b) A NW-SE seismic profile from the Omakere 3D seismic dataset across the Bear's Paw seep site and reflectivity anomaly to the NW of it (see (a) for the profile outline (white)), showing that the Bear's Paw seep site is characterized by a seafloor depression with underlying faults that deform the high amplitude reflections of HASRs 3. TWT[s]: Two-Way Time in Seconds.

Colored highlights in the multilevel RGB composed amplitude image (Figure 7d) represent the depth of elements that are presumably associated with the gas seepage system, based on the sub-windows used. For instance, the green color in the western end of the Kaka seep (Figure 7d) indicate the predominance of bright seismic reflections, representing probably seep-related features, within 4-15 ms below the seafloor. The bright cyan color at the eastern end of this seep (Figure 7d) indicates the deeper presence of intensely reflective features at the overlap of the 4-15 ms and 12-40 ms intervals below the seafloor. Together these may represent a lateral westward migration of gas in the sub-surface. The brightest reflections imaged in association with the seeps are cyan, suggesting that the primary gas accumulations are imaged ~15 ms below the surface. The overall intensity differs between the different seeps. Of the five verified seep sites in the study area, the dimmest composed amplitude response is associated with the Bear's Paw site, followed by the Kea seep site (Figure 7d). The brightest composed amplitude responses are associated with Kakapo (highest), Kaka, and the northern part of Moa (lowest). These responses are likely to be associated with seafloor and sub-seafloor features at the seep sites. This result contrasts previously published ranking based on surface observations. Bear's Paw and Kea sites were found to have the highest population densities of living chemosynthetic organisms, while having the least significant carbonate structures (Greinert et al., 2010; Jones et al., 2010). Moreover, Bear's Paw was found to have the highest methane concentrations in the water column, recorded up to several hundreds of meters above the seeps (Faure et al., 2010). On the other hand, the Kakapo, Kaka, and Moa seeps host the most significant carbonate structures and shells, as well as a variety of living seep-related biota, indicating long lasting to present-day activity (Jones et al., 2010). Based on these seafloor observations and results of sidescan sonar imaging, Jones et al. (2010) ranked the Bear's Paw seep as the most active seep, followed by Kea, the southwestern end of Moa, Kaka, Kakapo, and the northeastern end of Moa seeps (Figure 7d). Thus, the most active seeps with less cabonates match areas with dim composed amplitude responses, while the least active seeps with more carbonates match areas with bright composed amplitude responses (Figure 7d). It is possible that the multilevel composition response reflects the presence of seafloor authigenic carbonates and hardgrounds, which are generally characterized by high amplitude anomalies on seismic reflection data (Roberts et al., 2006). Alternatively, this discrepancy may be associated with the relatively large depth (~15 ms) of the brightest reflections, suggesting that the presently less active sites may be associated with deep accumulations of gas, while active sites are associated with smaller shallower gas accumulations. Taken together, these observations could suggest that past precipitation of pervasive authigenic carbonates sealed the now less active seepage site, while alternative interpretations may exist. Notably, the application of the multilevel composition technique highlighted this previously underappreciated discrepancy between the results of seismic imaging and seafloor observations.

Another significant result obtained by the multilevel composition technique in this area is the revelation that the Moa, Kakapo, and Kaka sites are each characterized by two distinct zones (Figure 7d). The Kakapo site consists of an eastern region with bright multilevel composed amplitude and a western region with dimmed multilevel composed amplitude. The Kaka site consists of an eastern end with dimmed composed amplitude and a western end with bright composed amplitude (Figure 7d). The Moa site is composed of a main northeastern region with bright composed amplitude and a southwestern region with dimmed composed amplitude (Figure 7d). These results of the multilevel composition at the Moa site favorably match seafloor observations of Jones et al. (2010). They show that the site is composed of a northeastern end with very high relief carbonate rocks, corals and non-seep fauna, and a southwestern end that supports chemosynthetic fauna. Consequently, our analysis indicates that the bright cyan (northwestern end) and dimmed (southwestern end) signals at the Moa site reflect the abundance of carbonate rocks at the northwestern end and their paucity at the southwestern ends, respectively. Based on these observations, it is suggested that like the Moa, the Kakapo and Kaka sites are perhaps made up of two zones with varying abundance of seep-related features and hence varying degree of activity.

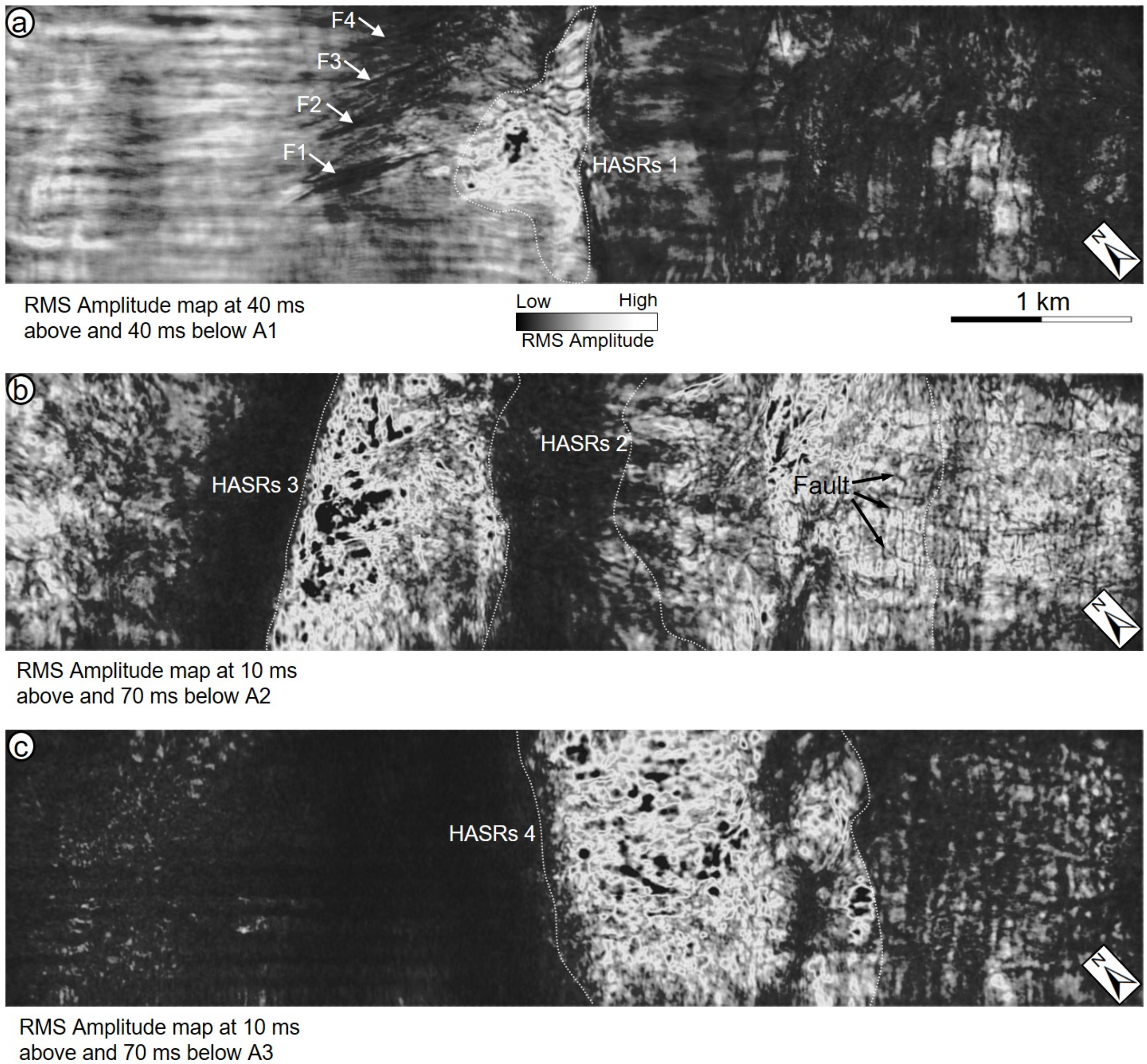

Figure 9. (a) A root mean square (RMS) amplitude map, extracted from 40 ms above to 40 ms below the A1 horizon in the Omakere 3D seismic dataset, highlighting the location and distribution of the anomalous reflections characterizing HASRs 1. Dark sub-parallel lines observed to the north of HASRs 1 represent faults: F1-F4. (b) A RMS amplitude map, extracted from 10 ms above to 70 ms below the A2 horizon, highlighting the distribution of anomalous reflections characterizing HASRs 3 and HASRs 2. Dark striping highlight multiple faults that

offset HASRs 2. (c) A RMS amplitude map, extracted from 10 ms above to 70 ms below horizon A3, highlighting the ~1 km wide N-S oriented HASRs 4.

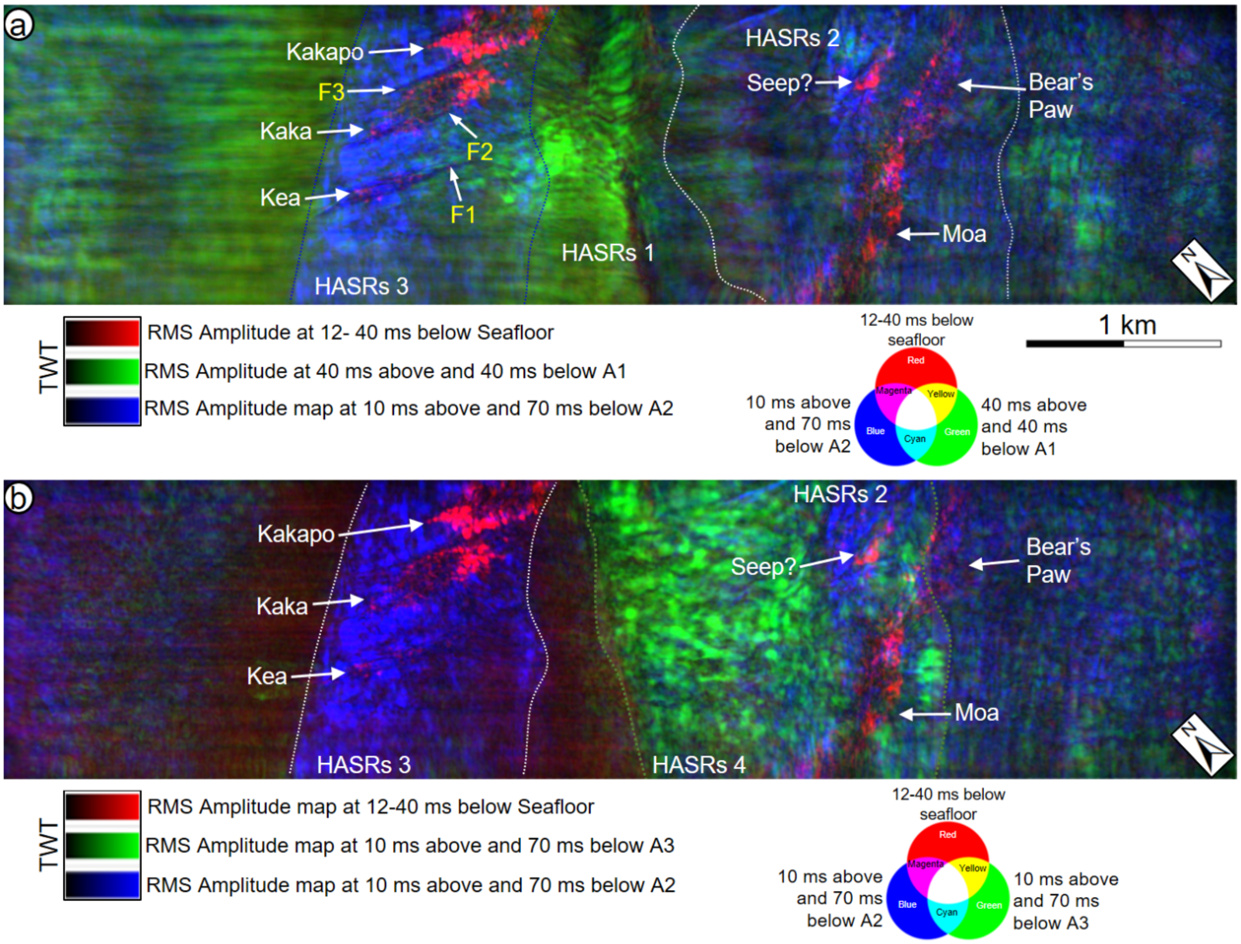

Figure 10. **(a)** A multilevel RGB composite of the amplitude maps in Figure 7c (12-40 ms below the seafloor, red), Figure 9a (40 ms above to 40 ms below horizon A1, green) and Fig 9b (10 ms above to 70 ms below horizon A2, blue). **(b)** A multilevel RGB composite of the amplitude maps Figure 7c (12-40 ms below the seafloor, red), Figure 9a (40 ms above to 40 ms below horizon A1, green), and Fig 9c (10 ms above to 70 ms below horizon A2, blue). For better imaging results the green represents here the deepest level, in difference with the other multilevel RGB composites presented in this paper. Note the enhanced illumination of the top, red, level of the multilevel amplitude responses below the seafloor seeps, as highlighted in cyan in Figure 7d. This reflectivity appear below the Kea, Kaka and Kakapo seeps to be spatially

related with faults F1-F4 and the overlap of the edges of HASRs 1 and HASRs 3. The Moa and Bear's Paw seeps, as well as the anomaly to the north of the latter, are spatially associated with the overlap of the edges of HASRs 2 and HASRs 4.

To investigate the connection of deeper reflections with the seafloor seeps a set of RMS amplitude maps were extracted with the reference horizons being A1, A2 and A3 (Figure 9). We find that HASRs 1 is located to the southeast of four near-parallel NW-SE oriented faults (F1-F4) and extends over an area of up to ~0.89 km^2 (Figure 9a). HASRs 2 and HASRs 3 extend over areas of 2.34 km^2 and 1.68 km^2 respectively in the vicinity of horizon A2, while HASRs 4 extends over an area of ~2.89 km^2 around horizon A3 (Figure 9b-c). Multilevel RGB compositions of these amplitude maps (Figure 10) help to constrain the relative positions of the deeper elements with respect to the seep areas (highlighted in red). We find that the Kea, Kaka and Kakapo seeps and their underlying near-parallel faults are directly spatially positioned above HASRs 3 (see the bright red color representing the seeps in Figure 10a). HASRs 1 overlaps with the southeastern edge of HASRs 3, with its edge underlying the northeastern seeps. However, it does not show any connection to HASRS 2 (Figure 10a). The edges of both HASRs 4 and HASRS 2 are overlapped beneath the Bear's Paw and Moa seeps (Figures 6b and 10b). Based on these observations, we infer that gas escaping from the Kea, Kaka and Kakapo seeps may be derived from the combination of fluids migrating from HASRs 3 and HASRs 1. Gases escaping at the Bear's Paw and Moa sites may be derived from the combination of fluids migrating from HASRs 4 and HASRs 2. Taken together the multilevel composition of amplitude maps (Figure 10) suggest that fluids are routed sub-vertically upward from deeper elements to the seeps. Beneath the Kea, Kaka, and Kakapo seeps this migration may be routed along faults F1-F4, as suggested by the alignment and spacing of the three seeps mimicking the style of the underlying faults F1-F4 (Figures 6b-c and 10).. Faults identified below the Moa and Bear's Paw seeps (Figures 6b and d and 9b) are suspected migration pathways for sub-vertical upward migration of fluids to shallower intervals below the Bear's Paw and Moa seeps.

5. Discussion

The case studies presented here provide basic demonstration of the utility of multilevel composition for robust visualization of the intricacy of complex geological features over a relative depth range in a single intuitive map. Dividing 3D seismic data into three sub-windows or depth intervals with respect to a sub-set of reference surfaces (commonly a signle surface). Assigning the red, green, and blue colors to attribute maps generated from the intervals and co-rendering them in the RGB color space, composes their attributes into a single map. The technique allows an interpreter to effectively visualize and characterize geological features and, importantly, to decode in colors normally hidden depth information. This is done with minimal effort, as only the reference horizon needs to be picked in a rigorous manner. The composed maps allow to derive high level morphological understandings, which delineate controlling processes, and can also be utilized to aid in more detailed mapping of complex reflectivity patterns.

Here we demonstrate the efficacy of the technique by combining multi-level amplitude maps in two different geological settings and types of datasets, and investigating two different processes. In the eastern Nile deep-sea fan, we interpreted standard commercial hydrocarbon exploration seismic data to characterize classical deep-water depositional elements with respect to the seafloor surface. The technique revealed depth-related information, which was used to infer evolution-related details about the depositional elements. We demonstrate the complementary utility of our new multilevel composition of amplitude maps with the commonly used and similarly looking spectral decomposition amplitude RGB composition. Spectral decomposition provides detailed structural information, associated with changes in thickness of the depositional features, while the multi-level composition constraines the relative positions of the different elements. In the Hikurangi Subduction Margin, we characterized seafloor cold seep sites and their underlying gas migration systems from 3D seismic images obtained by using high-resolution P-Cable seismic data. Here we used a combination of several different multi-level composition maps. In each example, the technique promoted the visual integration of three multilevel attribute maps at the same time. This greatly increased the value of the seismic attributes and enhanced visualization power. In the eastern Nile fan it deciphered the interdependence of multiple generations of the deep-sea channels system visualized, while highlighting a range of related depositional features. At the Omakere ridge, it was not only useful at detecting and characterizing seafloor seeps, but also at providing novel insights into their activity. Multilevel composition also indicated the likelihood of occurrence of a previously undiscovered seep site and highlighted close linkage between the Bear's Paw and Moa cold seep sites.

The multilevel composition provides a simple, mathematically straight-forward 5-step approach that works well in stratigraphically complex settings, where there are lateral facies variations and difficult-to-pick seismic horizons, similar to the Quaternary of the eastern Nile fan. It also works well in less complex settings where there is an interest in co-evaluation of multiple intervals, such as in the Omakere Ridge. The technique, as demonstrated here, will work adequately well where anomalous high amplitude features such as sand-bearing channels and lobes, blocky mass transport deposits, volcanics, carbonate-hosting seeps, hydrocarbon-bearing intervals and more stand out from the background data. However, the multi-level composition approach may be used for blending other attributes, further expanding its potential applicability.

The multilevel composition technique has therefore a broad scope of potential applications in basin analysis, subsurface resource, storage and sequestration assessment and characterization, offshore seep and minerals investigation, mapping of seafloor habitats, geohazard assessment for onshore and offshore sites and marine planning at large.

6. Conclusions

We propose here an innovative technique for 3D seismic interpretation, involving RGB composition and blending of multilevel attribute maps. The technique produces a single image map, in which inter-window/layer depth reflectivity information is coded in colors. This map characterizes the relative spatiotemporal distribution of intricate multi-depth geological features with respect to reference horizons. Here we demonstrate the efficacy of multilevel amplitude composition to characterize (a) buried channels and splay systems in the Eastern Nile fan in the Levant Basin, Eastern Mediterranean; and (b) cold seeps and their links to deeper gas-bearing intervals on the Omakere Ridge along the Hikurangi Margin, offshore New Zealand. We anticipate the multilevel composition approach to find wide application for studies linking several sub-surface depth levels, such as subsurface resource and storage characterization, fluid-flow related investigations, basin analysis, characterization of seafloor habitats and geohazard assessment.

Acknowledgments

This project was primarily funded by the State of Israel Ministry of Energy, contract no. 217-17-004, which is also acknowledged for granting permission for the Sara-Myra 3-D seismic dataset that is used in the Levant Basin case study; and by BIRD Foundation, US-Israel Energy Center, GoMed Fossil Fuels consortium. Funding for M. Lawal PhD was additionally granted by University of Haifa, and the Mediterranean Sea Research Center of Israel (MERCI). I. Pecher was partially funded by the New Zealand Ministry of Business, Innovation, and Employment contract CO5X1708 and a University of Auckland Grant in Aid to visit the University of Haifa. Special thanks to the crew and scientific team of R/V SONNE SO214 cruise to the Omakere Ridge, for acquiring the seismic data and granting permission to use it in this study. Voyage SO214 was supported by the German Federal Ministry for Education and Research (Bundesministerium für Bildung und Forschung, BMBF), project 03G0214. Dr Stefan Bünz, Univ. of Tromsø conducted much of the processing of the 3-D P-Cable data. We thank Emerson for providing us with licenses of Paradigm seismic interpretation and processing software.

Declaration of competing interests

The authors declare they have no known competing financial interests or personal relationships that could have appeared to influence the work reported in this paper.

Data Availability

The Sara-Myra (Levant Basin) seismic data used in this work is available, contingent on applied terms, from the Petroleum Commissioner Office, State of Israel Ministry of Energy. The Omakere Ridge (Hikurangi Margin) seismic data can be obtained, subject to approval, frm the cruise R/V SONNE SO214 team. Interpretation and attribute maps used to produce the figures of this paper can be made available, upon request, by the corresponding author.

References

Al-Shuhail, A.A., Al-Dossary, S.A., Mousa, W.A., 2017. Color Display of Seismic Images, in: Seismic Data Interpretation Using Digital Image Processing. https://doi.org/10.1002/9781119125594.ch6.

Alves, T.M., Omosanya, K., Gowling, P., 2015. Volume rendering of enigmatic high-amplitude anomalies in southeast Brazil: A workflow to distinguish lithologic features from fluid accumulations. Interpretation 3. https://doi.org/10.1190/INT-2014-0106.1.

Bacon, M., Simm, R., Redshaw, T., 2010. 3-D seismic interpretation, 3-D Seismic Interpretation. https://doi.org/10.1017/CBO9780511802416.

Bahorich, M., Farmer, S., 1995. The coherence cube. Lead. Edge 14, 1053–1058.

Barnes, P.M., Lamarche, G., Bialas, J., Henrys, S., Pecher, I., Netzeband, G.L., Greinert, J., Mountjoy, J.J., Pedley, K., Crutchley, G., 2010. Tectonic and geological framework for gas hydrates and cold seeps on the Hikurangi subduction margin, New Zealand. Mar. Geol. 272. https://doi.org/10.1016/j.margeo.2009.03.012.

Beavan, J., Tregoning, P., Bevis, M., Kato, T., Meertens, C., 2002. Motion and rigidity of the Pacific Plate and implications for plate boundary deformation. J. Geophys. Res. Solid Earth 107. https://doi.org/10.1029/2001jb000282.

Ben-Gai, Y., Ben-Avraham, Z., Buchbinder, B., Kendall, C.G.S.C., 2005. Post-Messinian evolution of the Southeastern Levant Basin based on two-dimensional stratigraphic simulation. Mar. Geol. https://doi.org/10.1016/j.margeo.2005.03.003.

Ben-Zeev, Y., Gvirtzman, Z., 2020. When Two Salt Tectonics Systems Meet: Gliding Downslope the Levant Margin and Salt Out-Squeezing From Under the Nile Delta. Tectonics 39. https://doi.org/10.1029/2019TC005715.

Bertoni, C., Cartwright, J.A., 2006. Controls on the basinwide architecture of late Miocene (Messinian) evaporites on the Levant margin (Eastern Mediterranean). Sediment. Geol. https://doi.org/10.1016/j.sedgeo.2006.03.019.

Brown, A.R., 2001. Understanding seismic attributes. Geophysics. https://doi.org/10.1190/1.1444919.

Brown, A.R., 1991. Interpretation of three-dimensional seismic data. Third edition. Interpret. three-dimensional Seism. data. Third Ed. https://doi.org/10.1190/1.9781560802884.

Buchbinder, B., Zilberman, E., 1997. Sequence stratigraphy of Miocene - Pliocene carbonate - Siliciclastic shelf deposits in the eastern Mediterranean margin (Israel): Effects of eustasy and tectonics. Sediment. Geol. https://doi.org/10.1016/S0037-0738(97)00034-1.

Burns, C.E., Mountney, N.P., Hodgson, D.M., Colombera, L., 2017. Anatomy and dimensions of fluvial crevasse-splay deposits: Examples from the Cretaceous Castlegate Sandstone and Neslen Formation, Utah, U.S.A. Sediment. Geol. 351. https://doi.org/10.1016/j.sedgeo.2017.02.003.

Cao, J., Yue, Y., Zhang, K., Yang, J., Zhang, X., 2015. Subsurface Channel Detection Using Color Blending of Seismic Attribute Volumes. Int. J. Signal Process. Image Process. Pattern Recognit. 8. https://doi.org/10.14257/ijsip.2015.8.12.16.

Cao, J., Zhang, X., Wang, Y., Zhao, Q., 2016. Subsurface geobody imaging using CMY color blending with seismic attributes. J. Electr. Comput. Eng. 2016. https://doi.org/10.1155/2016/9181254.

Cartwright, J., Huuse, M., 2005. 3D seismic technology: The geological "Hubble." Basin Res. https://doi.org/10.1111/j.1365-2117.2005.00252.x.

Cartwright, J., Jackson, M., Dooley, T., Higgins, S., 2012. Strain partitioning in gravity-driven shortening of a thick, multilayered evaporite sequence. Geol. Soc. Spec. Publ. https://doi.org/10.1144/SP363.21.

Cartwright, J.A., Jackson, M.P.A., 2008. Initiation of gravitational collapse of an evaporite basin margin: The Messinian saline giant, Levant Basin, eastern Mediterranean. Bull. Geol. Soc. Am. https://doi.org/10.1130/B26081X.1.

Chaves, M.U., Di Marco, L., Kawakami, G., Oliver, F., 2011. Visualization of Geological Features Using Seismic Volume Rendering, RGB Blending and Geobody Extraction. https://doi.org/10.1190/sbgf2011-175.

Chopra, S., Marfurt, K., 2006. Seismic Attributes – A Promising Aid for Geologic Prediction. CSEG Rec. 2006 Spec. Ed.

Chopra, S., Marfurt, K.J., 2008. Emerging and future trends in seismic attributes. Lead. Edge (Tulsa, OK). https://doi.org/10.1190/1.2896620.

Chopra, S., Marfurt, K.J., 2007. Seismic Attributes for Prospect Identification and Reservoir Characterization, Seismic Attributes for Prospect Identification and Reservoir Characterization. https://doi.org/10.1190/1.9781560801900.

Chopra, S., Marfurt, K.J., 2005. Seismic attributes - A historical perspective. Geophysics. https://doi.org/10.1190/1.2098670.

Clark, I.R., Cartwright, J.A., 2009. Interactions between submarine channel systems and deformation in deepwater fold belts: Examples from the Levant Basin, Eastern Mediterranean sea. Mar. Pet. Geol. https://doi.org/10.1016/j.marpetgeo.2009.05.004.

Clark, J.D., Kenyon, N.H., Pickering, K.T., 1992. Quantitative analysis of the geometry of submarine channels: implications for the classification of submarine fans. Geology 20. https://doi.org/10.1130/0091-7613(1992)020<0633:QAOTGO>2.3.CO;2.

Collot, J.Y., Delteil, J., Lewis, K.B., Davy, B., Lamarche, G., Audru, J.C., Barnes, P., Chanier, F., Chaumillon, E., Lallemand, S., De Lepinay, B.M., Orpin, A., Pelletier, B., Sosson, M., Toussaint, B., Uruski, C., 1996. From oblique subduction to intra-continental transpression: Structures of the southern Kermadec-Hikurangi margin from multibeam bathymetry, side-scan sonar and seismic reflection. Mar. Geophys. Res. 18.

https://doi.org/10.1007/BF00286085.

Di, H., Li, C., Smith, S., Abubakar, A., 2019. Machine learning-assisted seismic interpretation with geologic constraints, in: SEG Technical Program Expanded Abstracts. https://doi.org/10.1190/segam2019-w4-01.1.

Druckman, Y., Buchbinder, B., Martinotti, G.M., Tov, R.S., Aharon, P., 1995. The buried Afiq Canyon (eastern Mediterranean, Israel): a case study of a Tertiary submarine canyon exposed in Late Messinian times. Mar. Geol. https://doi.org/10.1016/0025-3227(94)00127-7.

Eruteya, O.E., Safadi, M., Waldmann, N., Makovsky, Y., Ben-Avraham, Z., 2016. Seismic geomorphology of the Israel slump complex in the Levant Basin (SE Mediterranean), in: Advances in Natural and Technological Hazards Research. https://doi.org/10.1007/978-3-319-20979-1_4.

Faure, K., Greinert, J., von Deimling, J.S., McGinnis, D.F., Kipfer, R., Linke, P., 2010. Methane seepage along the Hikurangi Margin of New Zealand: Geochemical and physical data from the water column, sea surface and atmosphere. Mar. Geol. 272. https://doi.org/10.1016/j.margeo.2010.01.001.

Folkman, Y., Mart, Y., 2008. Newly recognized eastern extension of the Nile deep-sea fan. Geology. https://doi.org/10.1130/G24995A.1.

Frey-Martínez, J., Cartwright, J., James, D., 2006. Frontally confined versus frontally emergent submarine landslides: A 3D seismic characterisation. Mar. Pet. Geol. https://doi.org/10.1016/j.marpetgeo.2006.04.002.

Frey-Martinez, J.F., Cartwright, J., Hall, B., 2005. 3D seismic interpretation of slump complexes: Examples from the continental margin of Israel. Basin Res.

https://doi.org/10.1111/j.1365-2117.2005.00255.x.

Gadol, O., Tibor, G., ten Brink, U., Hall, J.K., Groves-Gidney, G., Bar-Am, G., Hübscher, C., Makovsky, Y., 2019. Semi-automated bathymetric spectral decomposition delineates the impact of mass wasting on the morphological evolution of the continental slope, offshore Israel. Basin Res. bre.12420. https://doi.org/10.1111/bre.12420.

Gardosh, M.A., Druckman, Y., 2006. Seismic stratigraphy, structure and tectonic evolution of the Levantine Basin, offshore Israel. Geol. Soc. Spec. Publ. https://doi.org/10.1144/GSL.SP.2006.260.01.09.

Garfunkel, Z., 2004. Origin of the Eastern Mediterranean basin: A reevaluation. Tectonophysics. https://doi.org/10.1016/j.tecto.2004.07.006.

Greinert, J., Lewis, K.B., Bialas, J., Pecher, I.A., Rowden, A., Bowden, D.A., De Batist, M., Linke, P., 2010. Methane seepage along the Hikurangi Margin, New Zealand: Overview of studies in 2006 and 2007 and new evidence from visual, bathymetric and hydroacoustic investigations. Mar. Geol. 272. https://doi.org/10.1016/j.margeo.2010.01.017.

Gulliford, A.R., Flint, S.S., Hodgson, D.M., 2014. Testing applicability of models of distributive fluvial systems or trunk rivers in ephemeral systems: Reconstructing 3-D fluvial architecture in the Beaufort Group, South Africa. J. Sediment. Res. 84. https://doi.org/10.2110/jsr.2014.88.

Gvirtzman, Z., Manzi, V., Calvo, R., Gavrieli, I., Gennari, R., Lugli, S., Reghizzi, M., Roveri, M., 2017. Intra-Messinian truncation surface in the Levant Basin explained by subaqueous dissolution. Geology. https://doi.org/10.1130/G39113.1.

Gvirtzman, Z., Reshef, M., Buch-Leviatan, O., Groves-Gidney, G., Karcz, Z., Makovsky, Y., Ben-Avraham, Z., 2015. Bathymetry of the Levant basin: Interaction of salt-tectonics and surficial mass movements. Mar. Geol. https://doi.org/10.1016/j.margeo.2014.12.001.

Henderson, J., Purves, S.J., Fisher, G., 2008. Delineation of geological elements from RGB color blending of seismic attribute volumes. Lead. Edge (Tulsa, OK) 27. https://doi.org/10.1190/1.2896625.

Janocko, M., Nemec, W., Henriksen, S., Warchoł, M., 2013. The diversity of deep-water sinuous channel belts and slope valley-fill complexes. Mar. Pet. Geol. 41. https://doi.org/10.1016/j.marpetgeo.2012.06.012.

Jolly, B.A., Lonergan, L., Whittaker, A.C., 2016. Growth history of fault-related folds and interaction with seabed channels in the toe-thrust region of the deep-water Niger delta. Mar. Pet. Geol. 70. https://doi.org/10.1016/j.marpetgeo.2015.11.003.

Jones, A.T., Greinert, J., Bowden, D.A., Klaucke, I., Petersen, C.J., Netzeband, G.L., Weinrebe, W., 2010. Acoustic and visual characterisation of methane-rich seabed seeps at Omakere Ridge on the Hikurangi Margin, New Zealand. Mar. Geol. 272. https://doi.org/10.1016/j.margeo.2009.03.008.

Judd, A., Hovland, M., 2007. Seabed fluid flow: The impact on geology, biology, and the marine environment, Seabed Fluid Flow: The Impact on Geology, Biology, and the Marine Environment. https://doi.org/10.1017/CBO9780511535918.

Kanari, M., Tibor, G., Hall, J.K., Ketter, T., Lang, G., Schattner, U., 2020. Sediment transport mechanisms revealed by quantitative analyses of seafloor morphology: New evidence from multibeam bathymetry of the Israel exclusive economic zone. Mar. Pet. Geol. 114. https://doi.org/10.1016/j.marpetgeo.2020.104224.

Katz, O., Reuven, E., Aharonov, E., 2015. Submarine landslides and fault scarps along the eastern Mediterranean Israeli continental-slope. Mar. Geol. 369.

https://doi.org/10.1016/j.margeo.2015.08.006.
Kolla, V., Posamentier, H.W., Wood, L.J., 2007. Deep-water and fluvial sinuous channels-Characteristics, similarities and dissimilarities, and modes of formation. Mar. Pet. Geol. https://doi.org/10.1016/j.marpetgeo.2007.01.007.

Koson, S., Chenrai, P., Choowong, M., 2014. Seismic Attributes and Their Applications in Seismic Geomorphology. Bull. Earth Sci. Thail.

Kumar, P.C., Sain, K., 2020. A machine learning tool for interpretation of Mass Transport Deposits from seismic data. Sci. Rep. 10. https://doi.org/10.1038/s41598-020-71088-6.

Macgregor, D.S., 2012. The development of the Nile drainage system: Integration of onshore and offshore evidence. Pet. Geosci. https://doi.org/10.1144/petgeo2011-074.

Marfurt, K.J., 2015. Techniques and best practices in multiattribute display. Interpretation 3. https://doi.org/10.1190/INT-2014-0133.1.

Meilijson, A., Hilgen, F., Sepúlveda, J., Steinberg, J., Fairbank, V., Flecker, R., Waldmann, N.D., Spaulding, S.A., Bialik, O.M., Boudinot, F.G., Illner, P., Makovsky, Y., 2019. Chronology with a pinch of salt: Integrated stratigraphy of Messinian evaporites in the deep Eastern Mediterranean reveals long-lasting halite deposition during Atlantic connectivity. Earth-Science Rev. https://doi.org/10.1016/j.earscirev.2019.05.011.

Netzeband, G.L., Hübscher, C.P., Gajewski, D., 2006. The structural evolution of the Messinian evaporites in the Levantine Basin. Mar. Geol. https://doi.org/10.1016/j.margeo.2006.05.004.

Nicol, A., Mazengarb, C., Chanier, F., Rait, G., Uruski, C., Wallace, L., 2007. Tectonic evolution of the active Hikurangi subduction margin, New Zealand, since the Oligocene. Tectonics 26. https://doi.org/10.1029/2006TC002090.

Niyazi, Y., Eruteya, O.E., Omosanya, K.O., Harishidayat, D., Johansen, S.E., Waldmann, N.,

2018. Seismic geomorphology of submarine channel-belt complexes in the Pliocene of the Levant Basin, offshore central Israel. Mar. Geol. https://doi.org/10.1016/j.margeo.2018.05.007.

Özsoy, E., Hecht, A., Ünlüata, Ü., Brenner, S., Sur, H.I., Bishop, J., Latif, M.A., Rozentraub, Z., Oğuz, T., 1993. A synthesis of the Levantine Basin circulation and hydrography, 1985-1990. Deep. Res. Part II. https://doi.org/10.1016/0967-0645(93)90063-S.

Partyka, G., Gridley, J., Lopez, J., 1999. Interpretational applications of spectral decomposition in reservoir characterization. Lead. Edge. https://doi.org/10.1190/1.1438295.

Peakall, J., Kane, I.A., Masson, D.G., Keevil, G., Mccaffrey, W., Corney, R., 2012. Global (latitudinal) variation in submarine channel sinuosity. Geology 40. https://doi.org/10.1130/G32295.1.

Pecher, I.A., Henrys, S.A., Wood, W.T., Kukowski, N., Crutchley, G.J., Fohrmann, M., Kilner, J., Senger, K., Gorman, A.R., Coffin, R.B., Greinert, J., Faure, K., 2010. Focussed fluid flow on the Hikurangi Margin, New Zealand — Evidence from possible local upwarping of the base of gas hydrate stability. Mar. Geol. 272, 99–113. https://doi.org/10.1016/j.margeo.2009.10.006.

Plaza-Faverola, A., Pecher, I., Crutchley, G., Barnes, P.M., Bünz, S., Golding, T., Klaeschen, D., Papenberg, C., Bialas, J., 2014. Submarine gas seepage in a mixed contractional and shear deformation regime: Cases from the Hikurangi oblique-subduction margin. Geochemistry, Geophys. Geosystems 15. https://doi.org/10.1002/2013GC005082.

Posamentier, H.W., 2003. Depositional elements associated with a basin floor channel-levee system: Case study from the Gulf of Mexico. Mar. Pet. Geol. 20. https://doi.org/10.1016/j.marpetgeo.2003.01.002.

Posamentier, H.W., Kolla, V., 2003. Seismic Geomorphology and Stratigraphy of Depositional Elements in Deep-Water Settings. J. Sediment. Res. https://doi.org/10.1306/111302730367.

Reiche, S., Hübscher, C., Brenner, S., Betzler, C., Hall, J.K., 2018. The role of internal waves in the late Quaternary evolution of the Israeli continental slope. Mar. Geol. 406. https://doi.org/10.1016/j.margeo.2018.09.013.

Roberts, H.H., Hardage, B.A., Shedd, W.W., Hunt, J., 2006. Seafloor reflectivity - An important seismic property for interpreting fluid/gas expulsion geology and the presence of gas hydrate. Lead. Edge. https://doi.org/10.1190/1.2202667.

Roveri, M., Flecker, R., Krijgsman, W., Lofi, J., Lugli, S., Manzi, V., Sierro, F.J., Bertini, A., Camerlenghi, A., De Lange, G., Govers, R., Hilgen, F.J., Hübscher, C., Meijer, P.T., Stoica, M., 2014. The Messinian Salinity Crisis: Past and future of a great challenge for marine sciences. Mar. Geol. https://doi.org/10.1016/j.margeo.2014.02.002.

Sagy, Y., Dror, O., Gardosh, M., Reshef, M., 2020. The origin of the Pliocene to recent succession in the Levant basin and its depositional pattern, new insight on source to sink system. Mar. Pet. Geol. 120, 104540. https://doi.org/10.1016/j.marpetgeo.2020.104540.

Schattner, U., Lang, G., Lazar, M., 2017. Pliocene or Pleistocene, That Is the Question – New Constraints from the Eastern Mediterranean, in: Quaternary of the Levant. https://doi.org/10.1017/9781316106754.007.

Schattner, U., Lazar, M., 2016. Hierarchy of source-to-sink systems — Example from the Nile distribution across the eastern Mediterranean. Sediment. Geol. https://doi.org/10.1016/j.sedgeo.2016.08.006.

Stark, T.J., 2006. Visualization techniques for enhancing stratigraphic inferences from 3D seismic data volumes. First Break 24. https://doi.org/10.1524/icom.2006.5.1.75.

Subrahmanyam, D., Rao, P.H., 2008. Seismic Attributes-A Review, in: 7th International Conference and Exposition on Petroleum Geophysics.

Taner, M.T., Koehler, F., Sheriff, R.E., 1979. COMPLEX SEISMIC TRACE ANALYSIS. Geophysics 44. https://doi.org/10.1190/1.1440994.

Tayber, Z., Meilijson, A., Ben-Avraham, Z., Makovsky, Y., 2019. Methane Hydrate Stability and Potential Resource in the Levant Basin, Southeastern Mediterranean Sea. Geosciences 9, 306. https://doi.org/10.3390/geosciences9070306.

Wallace, L.M., Barnes, P., Beavan, J., Van Dissen, R., Litchfield, N., Mountjoy, J., Langridge, R., Lamarche, G., Pondard, N., 2012. The kinematics of a transition from subduction to strike-slip: An example from the central New Zealand plate boundary. J. Geophys. Res. Solid Earth 117. https://doi.org/10.1029/2011JB008640.

Watson, S.J., Mountjoy, J.J., Barnes, P.M., Crutchley, G.J., Lamarche, G., Higgs, B., Hillman, J., Orpin, A.R., Micallef, A., Neil, H., Mitchell, J., Pallentin, A., Kane, T., Woelz, S., Bowden, D., Rowden, A.A., Pecher, I.A., 2020. Focused fluid seepage related to variations in accretionary wedge structure, hikurangi margin, New Zealand. Geology 48. https://doi.org/10.1130/G46666.1.

Zeng, H., 2010. Stratal slicing: Benefits and challenges. Lead. Edge (Tulsa, OK) 29. https://doi.org/10.1190/1.3485764.

Zheng, Y., Zhang, Q., Yusifov, A., Shi, Y., 2019. Applications of supervised deep learning for seismic interpretation and inversion. Lead. Edge 38. https://doi.org/10.1190/tle38070526.1.

Zucker, E., Gvirtzman, Z., Granjeon, D., Garcia-Castellanos, D., Enzel, Y., 2021. The accretion of the Levant continental shelf alongside the Nile Delta by immense margin-parallel sediment transport. Mar. Pet. Geol. 126. https://doi.org/10.1016/j.marpetgeo.2020.104876.

Zucker, E., Gvirtzman, Z., Steinberg, J., Enzel, Y., 2020. Salt tectonics in the Eastern Mediterranean Sea: Where a giant delta meets a salt giant. Geology. https://doi.org/10.1130/g47031.1.

Zucker, E., Gvirtzman, Z., Steinberg, J., Enzel, Y., 2017. Diversion and morphology of submarine channels in response to regional slopes and localized salt tectonics, Levant Basin. Mar. Pet. Geol. https://doi.org/10.1016/j.marpetgeo.2017.01.002.

Supplementary Information

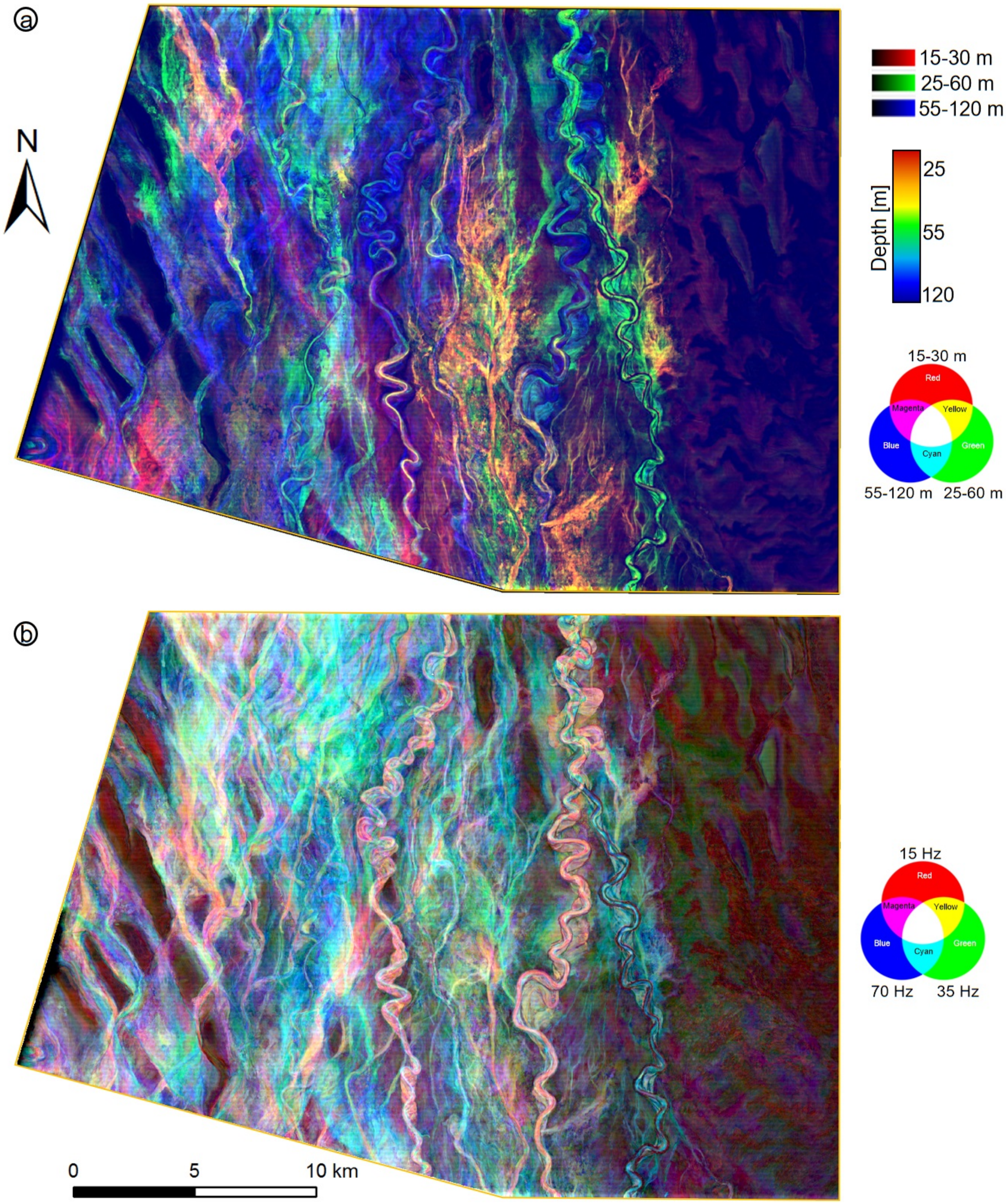

Supplementary Figure 1. (a) A multilevel RGB composite image of signal-envelope maps extracted from the Sara-Mira 3D seismic dataset for the 15-30 m (red), 25-60 m (green), and 55-120 m (blue) below the seafloor (color coding in the upper right). The lower right color bar estimates the depth below the seafloor, which is reflected by the combined colors of the image. The image delineates the relative stratigraphic position of paleo-channels and splays and their interactions, and helps to constrain the evolution of this system. (b) An RGB composite image of spectral decomposition results over the same 15 to 120 m interval below the seafloor, combining the 15 Hz (red), 35 Hz (green), and 70 Hz (blue) central frequency bands (color coding on the right). This image delineates the same features as in (a), color coded in relation primarily to their thickness.